

Figure 7.13

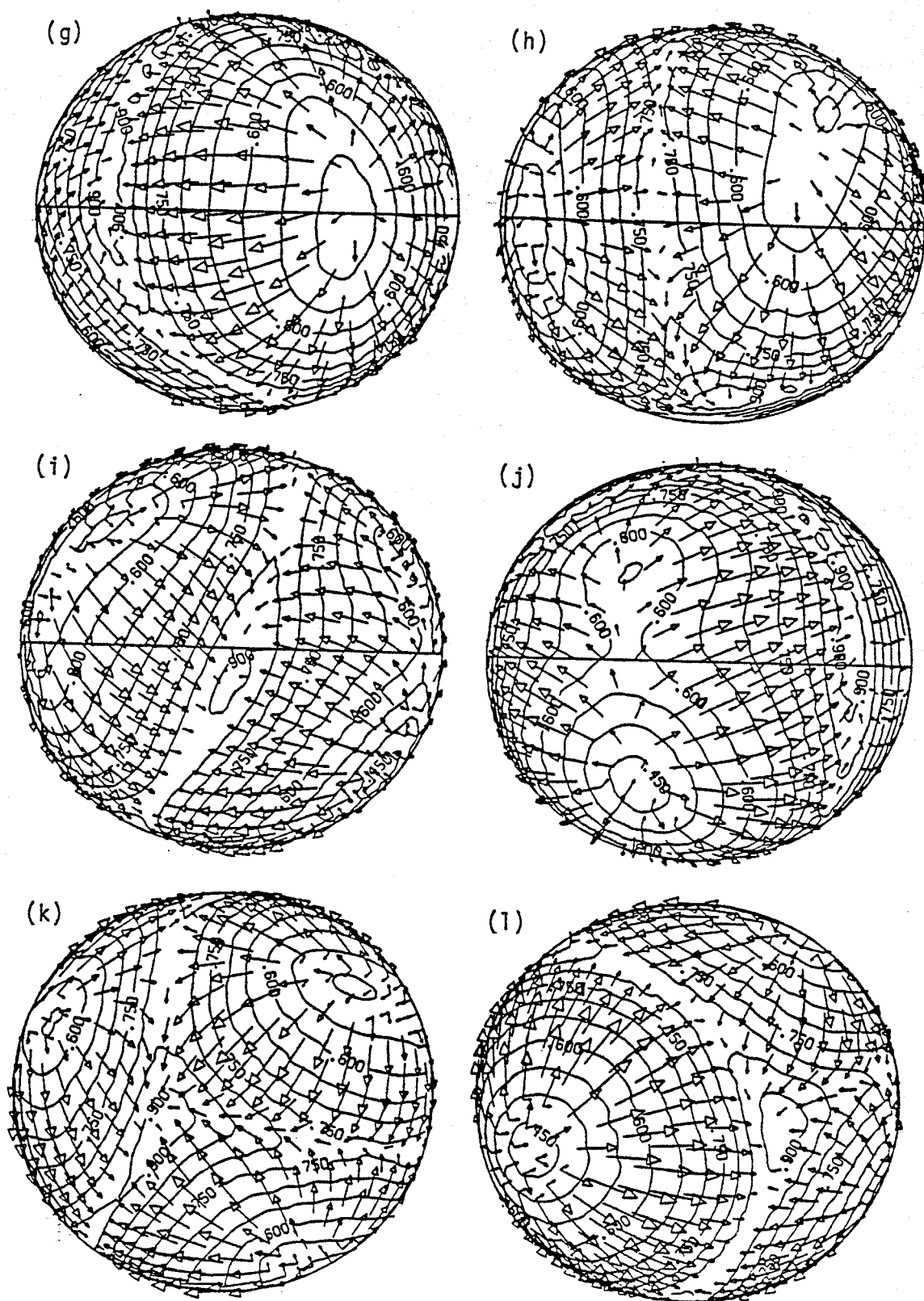


Figure 7.13

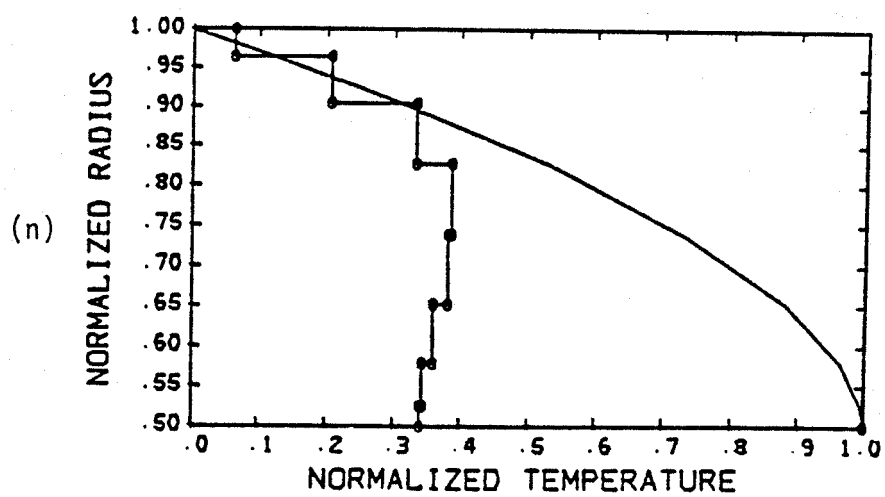
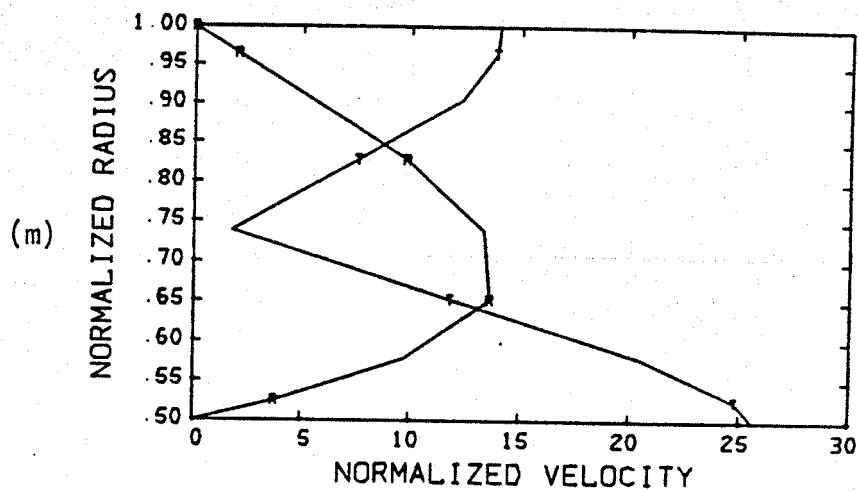


Figure 7.13

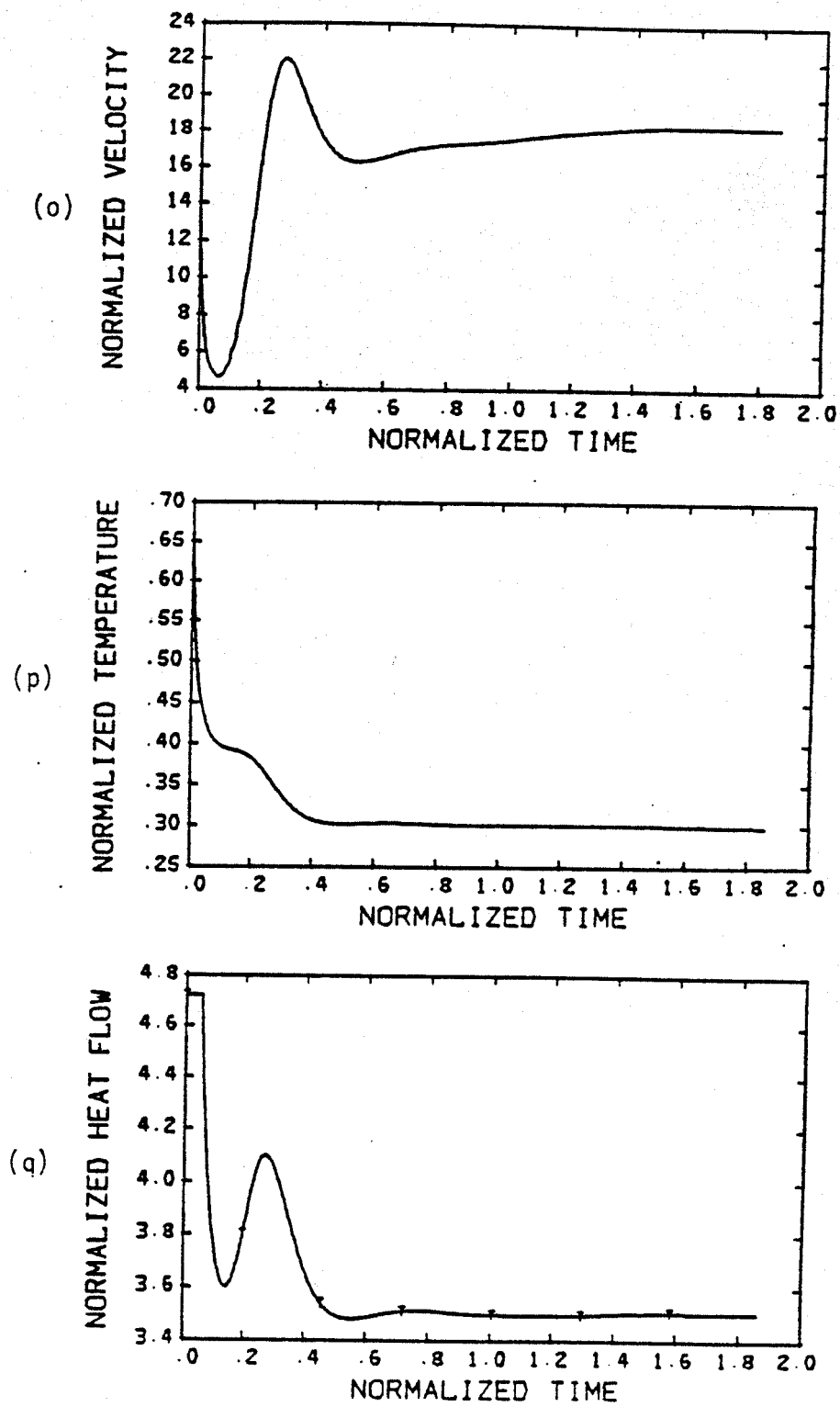


Figure 7.13

Figure 7.14. Convection solution for spherical shell, radius ratio 0.50, Rayleigh number 100,000, heated only from within, with gravitational acceleration increasing linearly with radius and initialized with a random temperature distribution. Final velocity and temperature fields are displayed in (a)-(l). Orientations and radial positions of views are identical to those of Figure 7.2. Maximum velocity for views (a)-(f) is 50.4 and for views (g)-(l) is 84.3. (m)-(q) correspond to similar plots in Figure 7.12.

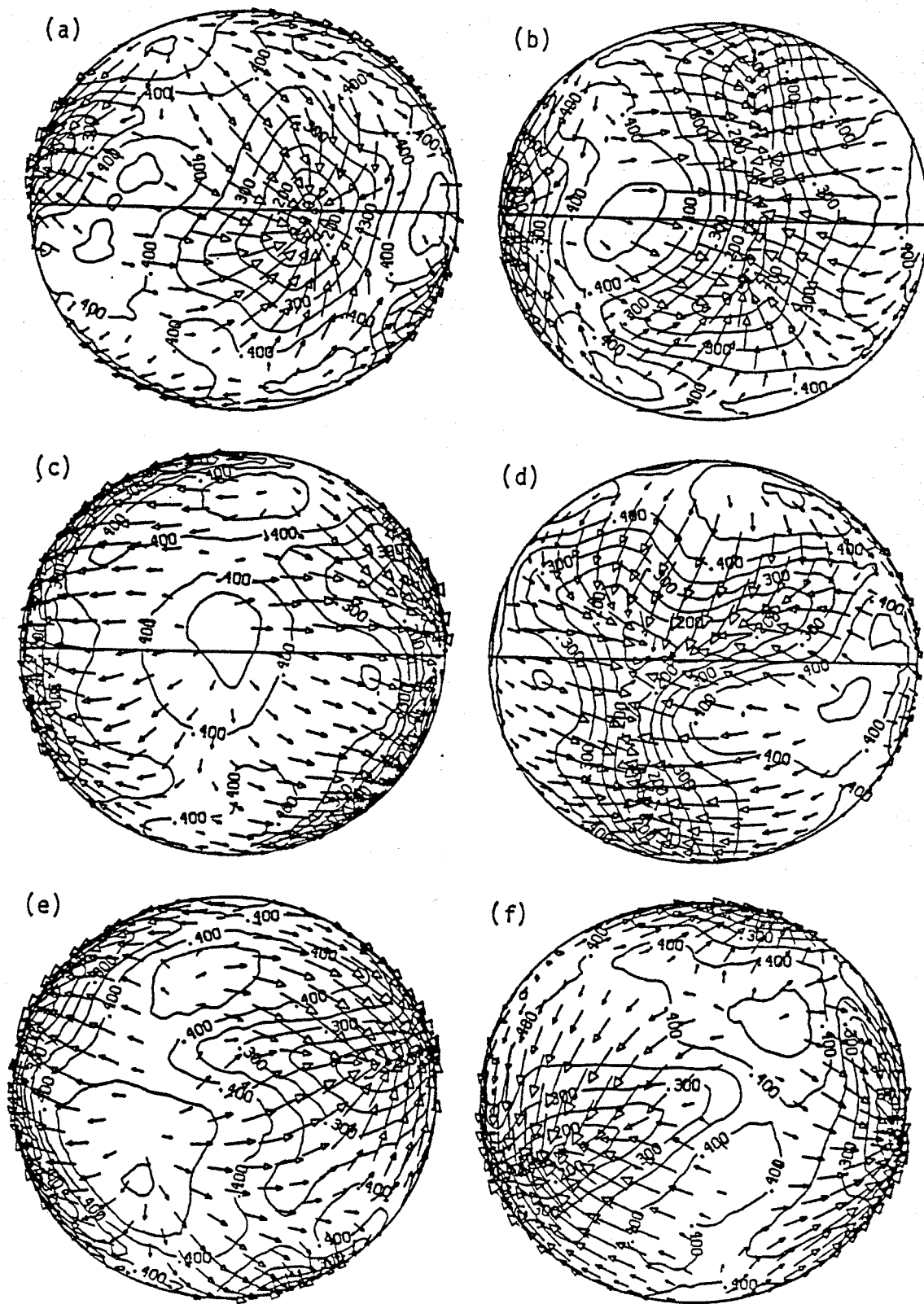


Figure 7.14

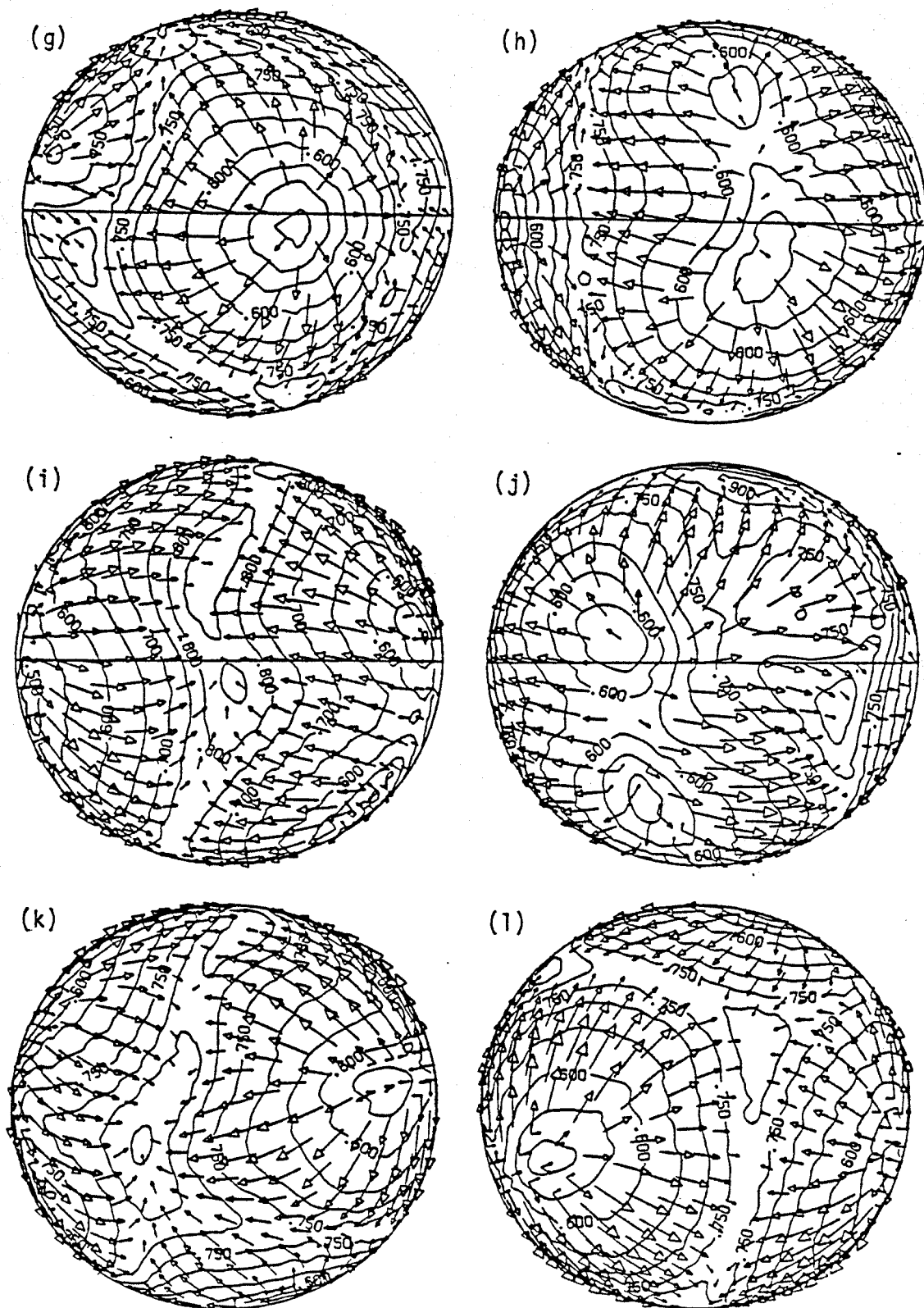


Figure 7.14

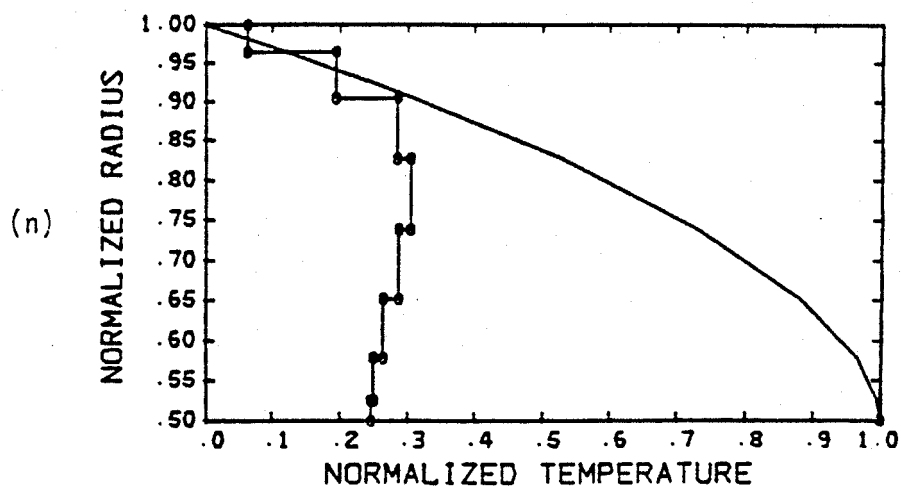
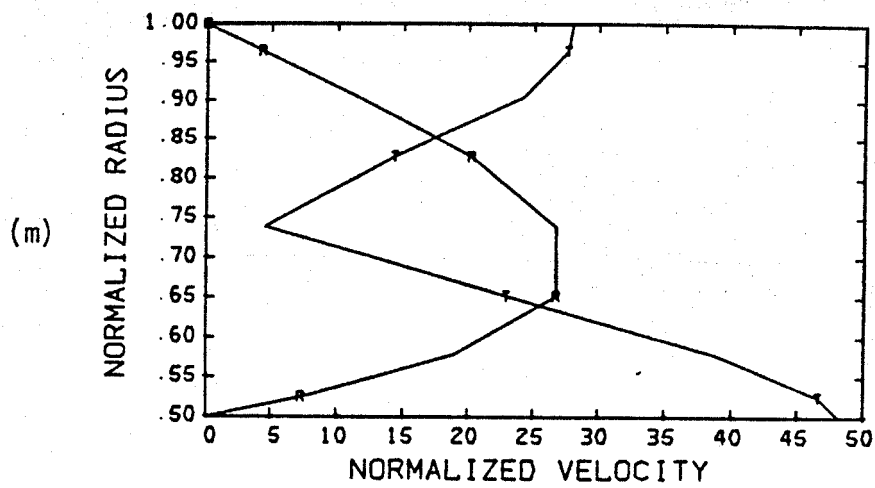


Figure 7.14

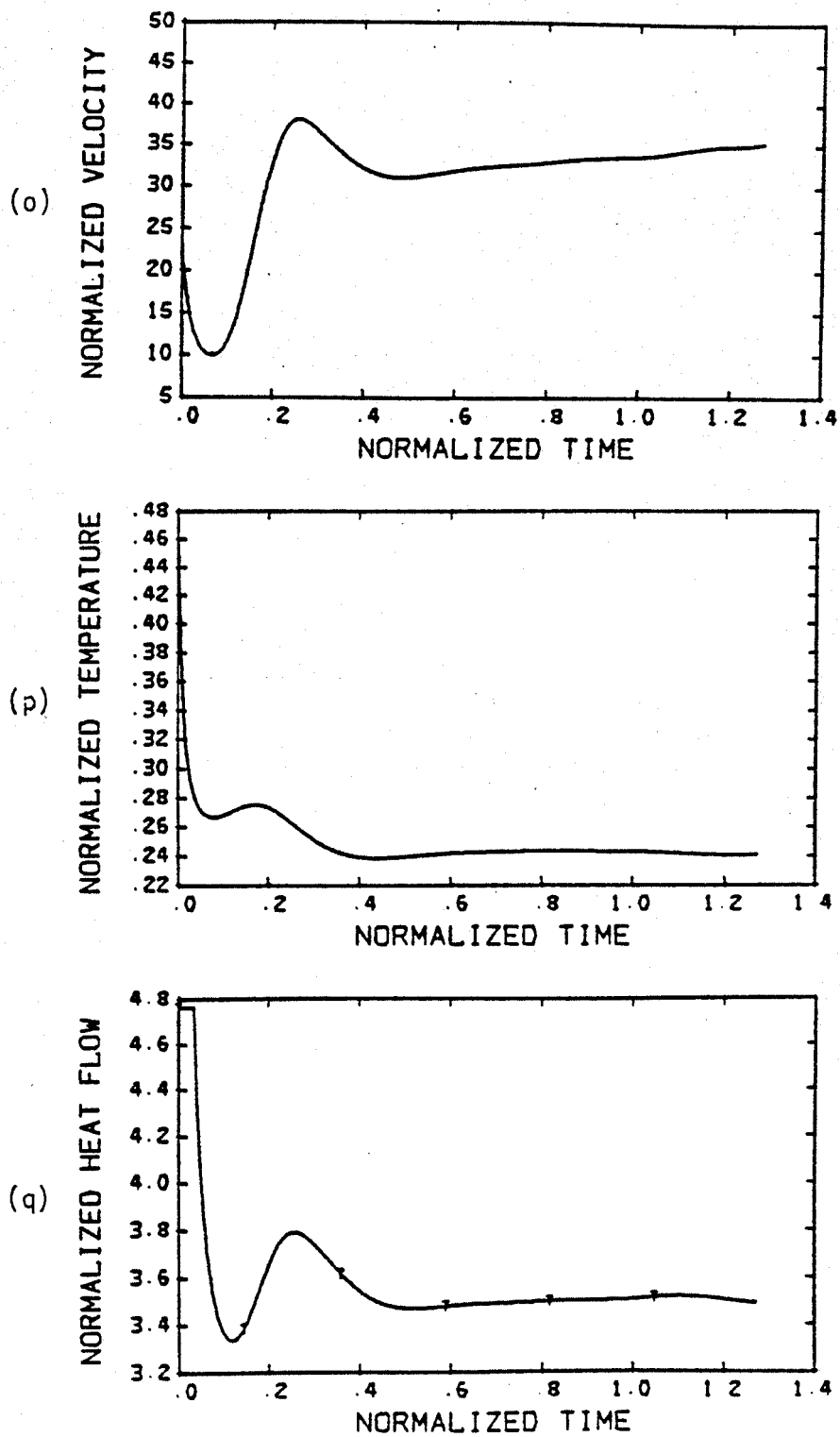


Figure 7.14

Figure 7.15. Convection solution for spherical shell, radius ratio 0.50, Rayleigh number 300,000, heated only from within, with gravitational acceleration increasing linearly with radius and initialized with a random temperature distribution. Final velocity and temperature fields are displayed in (a)-(l). Orientations and radial positions of views are identical with those of Figure 7.2. Maximum velocity for views (a)-(f) is 92.5 and for views (g)-(l) is 131.5. (m)-(q) correspond to similar plots in Figure 7.12.

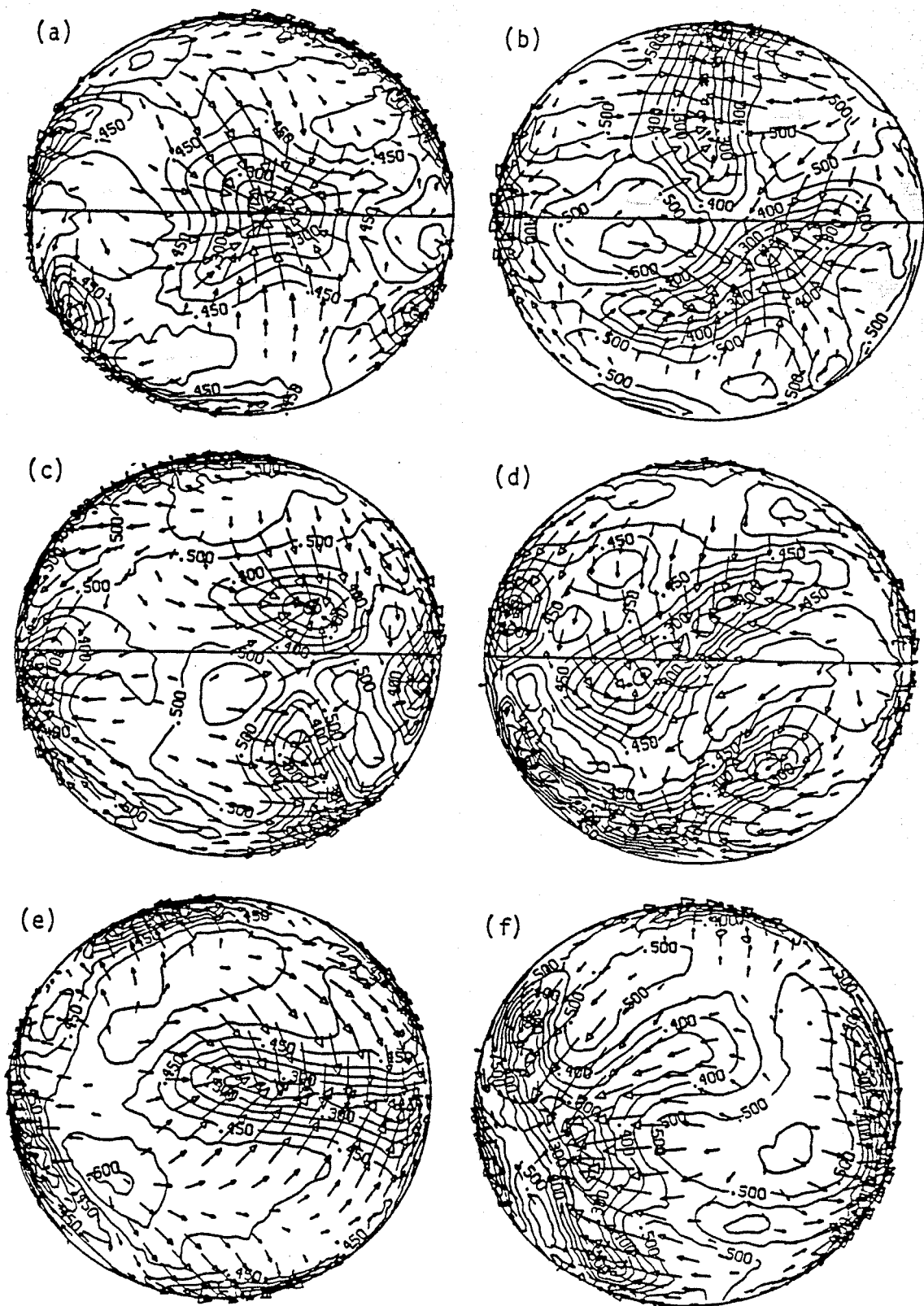


Figure 7.15

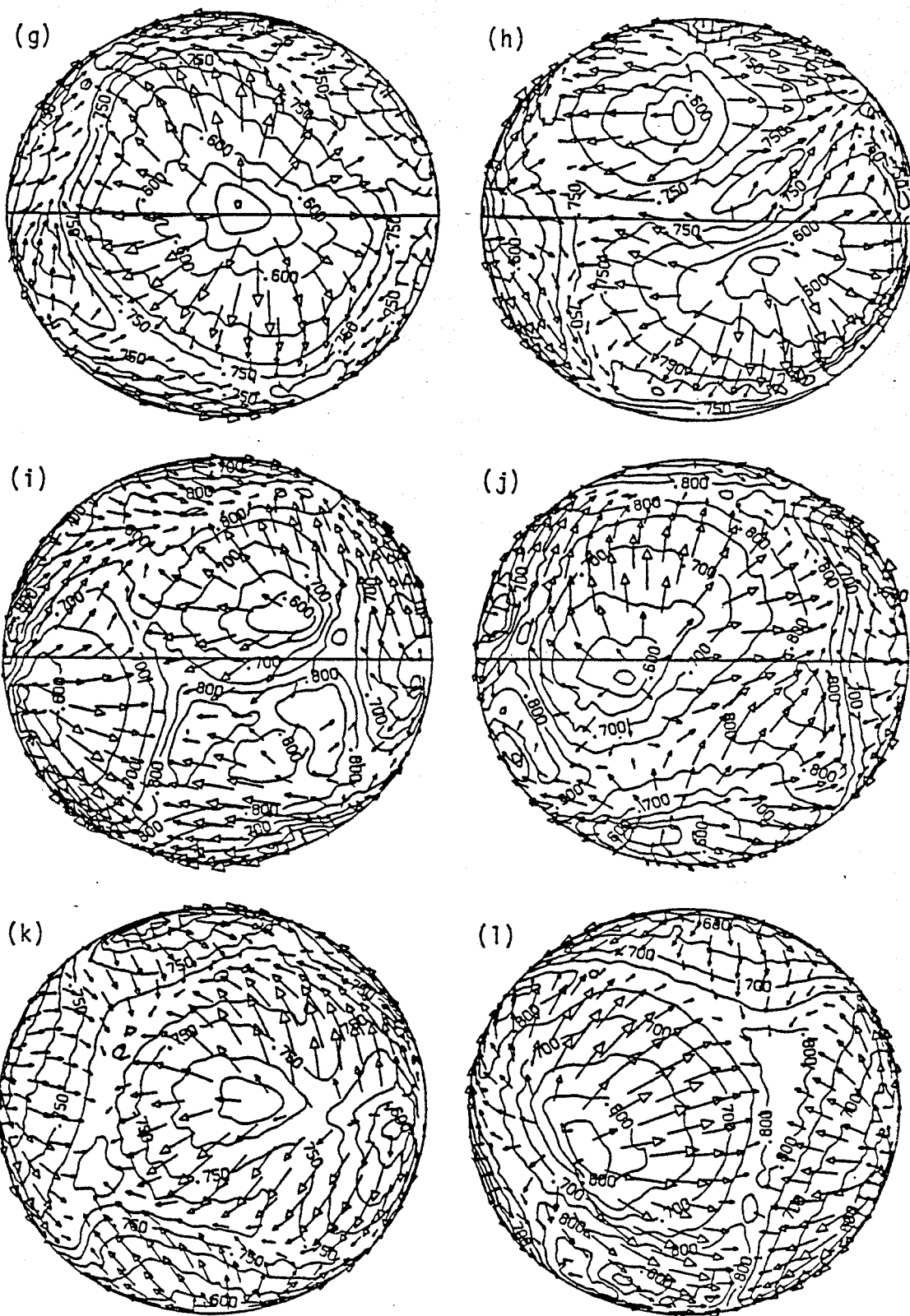


Figure 7.15

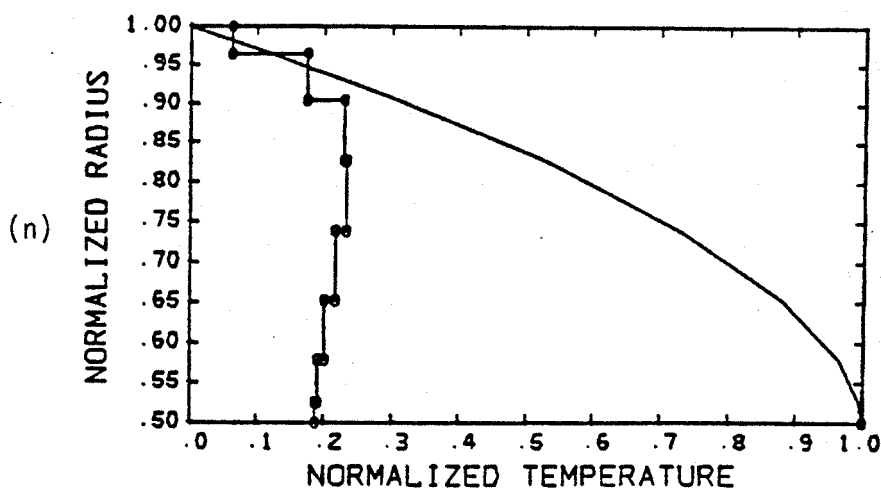
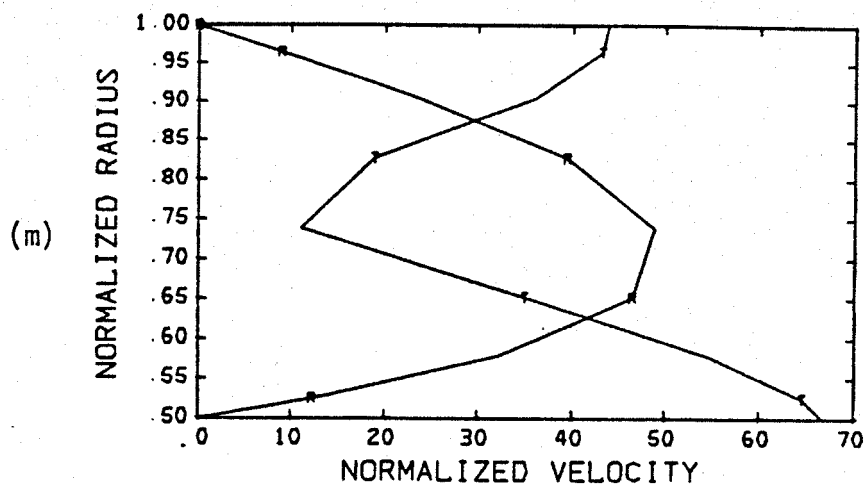


Figure 7.15

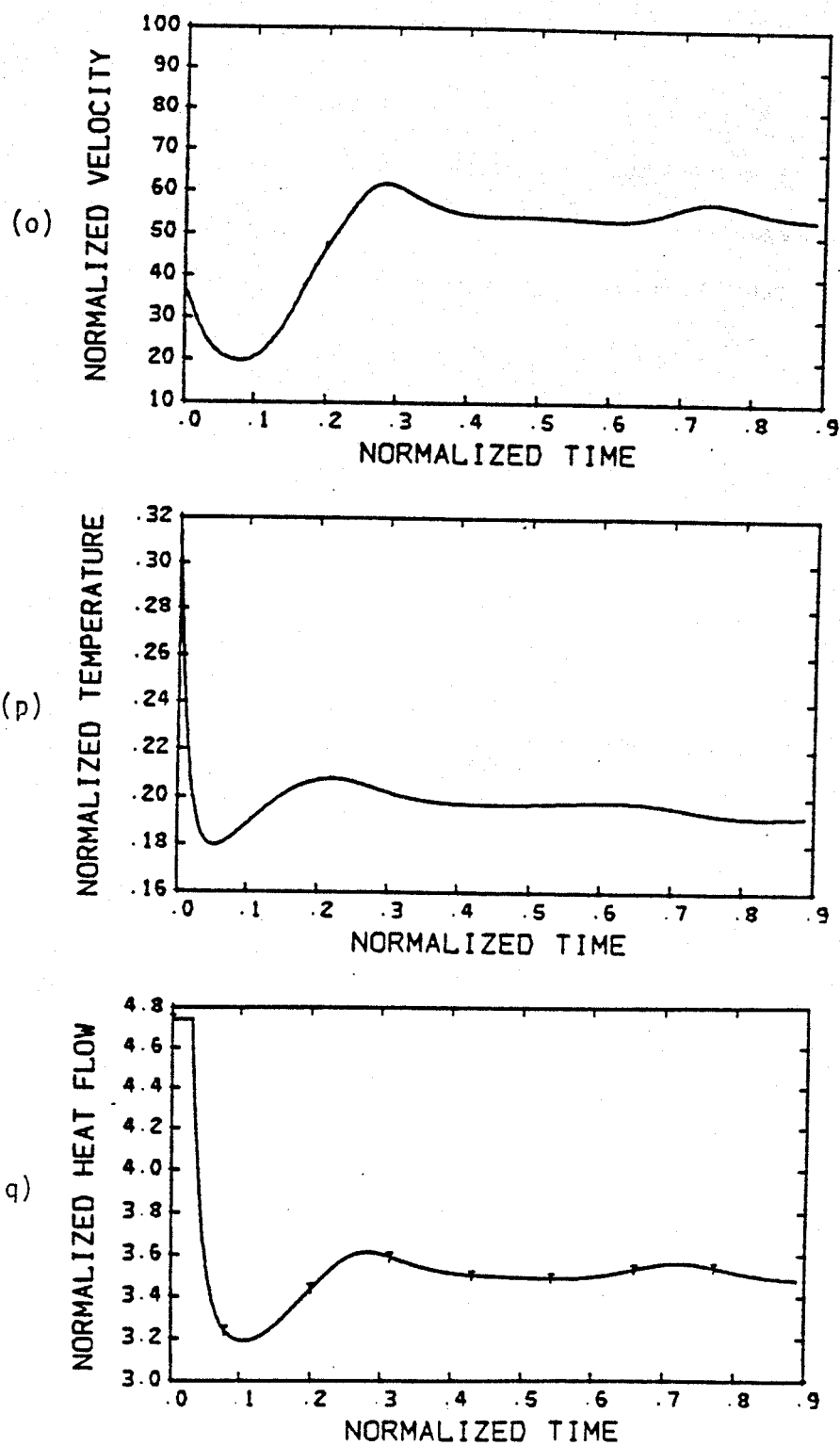


Figure 7.15

7.4 SHELL HEATED BOTH FROM BELOW AND FROM WITHIN

The final experiment to be described in this chapter allows the inner boundary to be conducting and examines the effect of varying amounts of internal heat on the pattern of convective flow. In this experiment the conditions used for the $R = 25,000$ heated from below case of Section 7.2 are retained except that internal heating is added. The preferred solution corresponding to Figure 7.2 is used as the initial condition. Three cases are described for which the fraction of internally generated heat of the total heat flux leaving the shell is approximately 25, 50, and 75 percent.

Figures 7.16 and 7.17 display the temperature and velocity fields for the 50 and 75 percent cases, respectively. In the case of 50% internal heating, the cells show some distortion in shape compared with the pattern of Figure 7.2, but otherwise the cell sizes and locations are essentially the same. However, when the internal heating is increased to 75%, notable changes occur. At the outer boundary, although three regions of upwelling flow may still be identified, the pattern is dominated by two intense linear zones of downwelling flow, more or less orthogonal to one another and on opposite sides of the sphere. At the inner boundary, the pattern consists of two large cells with downwelling at their centers and a continuous zone of upwelling suggestive of the seams on a baseball or tennis ball. The effect of the internal heating seems to make the regions of upwelling in the outer portions of the shell more diffuse, while making the downwelling more localized and intense. The heat from below, at this Rayleigh number at least, appears to be keeping the pattern organized in a regular and orderly fashion in a small number of cells.

Figure 7.18 shows the spherically averaged radial temperature distributions for these three cases. There is a clear correspondence between the fraction of internal heating and the interior temperature of the shell. If the heating from below is neglected and the Rayleigh number formula (7.2) for an exclusively internally heated shell is applied to these three cases, the resulting Rayleigh numbers are 30,600, 80,000, and 162,000, respectively. The fact that interior temperatures of the 50 and 75 percent cases are much higher than those obtained in the preceding section at comparable Rayleigh numbers with strictly internal heating indicates that a modest amount of heating from below exerts a strong influence on the convective process.

Figure 7.19 shows the spherically averaged radial and tangential velocity profiles versus radius. Although the normalized heat flows for these cases are 5.86, 7.47, and 10.17, respectively, the velocity profiles hardly differ. These cases suggest that partial internal heating, compared with heating only from below, raises the internal temperature, increases the outflow of heat, alters the pattern somewhat, but leaves the mean convective velocities essentially unchanged.

Figure 7.16. Convection solution for spherical shell, radius ratio 0.50, Rayleigh number 25,000, 50% internal heating, with gravitational acceleration increasing linearly with radius and initialized with preferred pattern. Velocity and temperature fields are displayed in (a)-(l). Orientations and radial positions of views are identical to those of Figure 7.2. Maximum velocity for views (a)-(f) is 89.5 and for views (g)-(l) is 151.8.

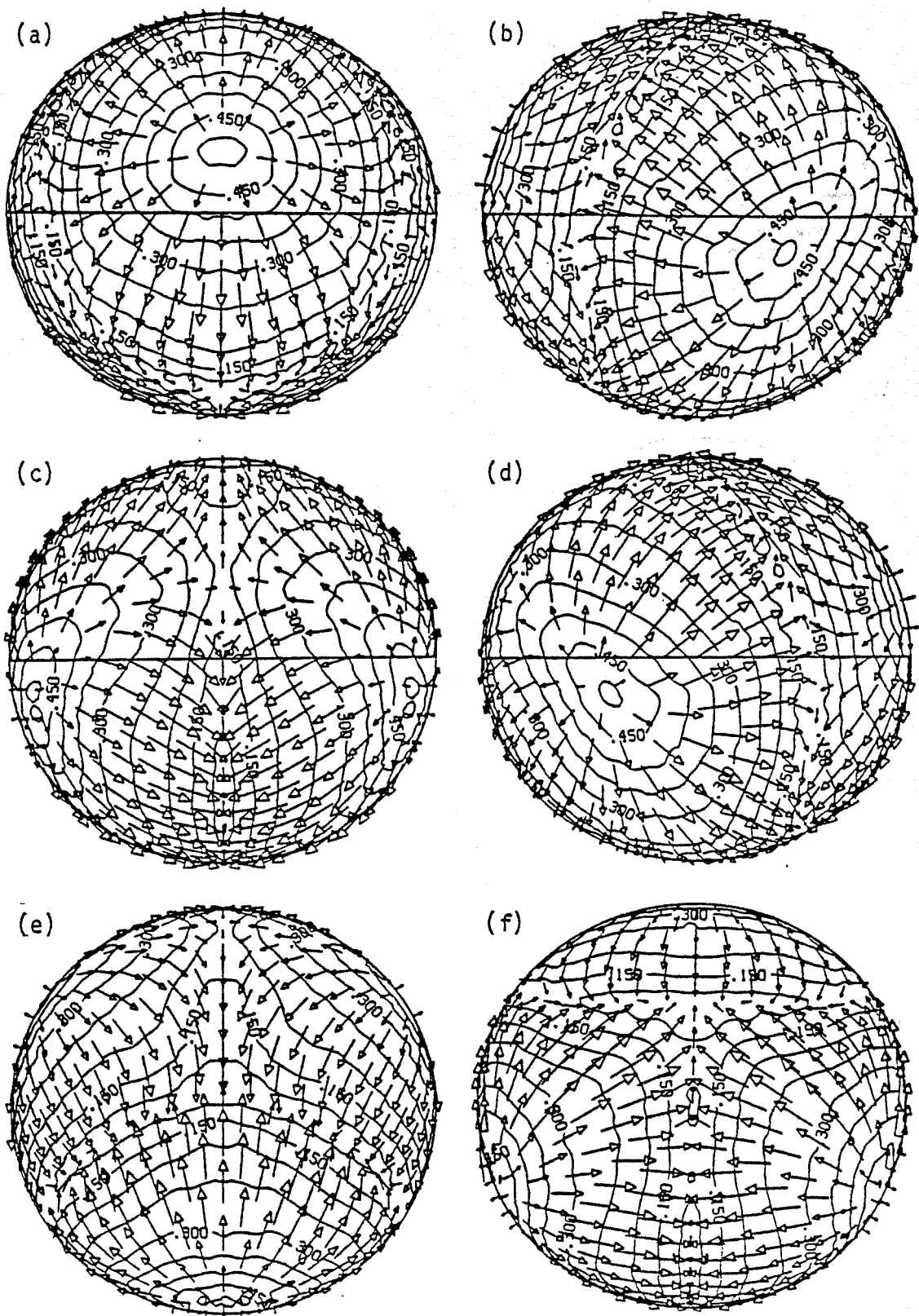


Figure 7.16

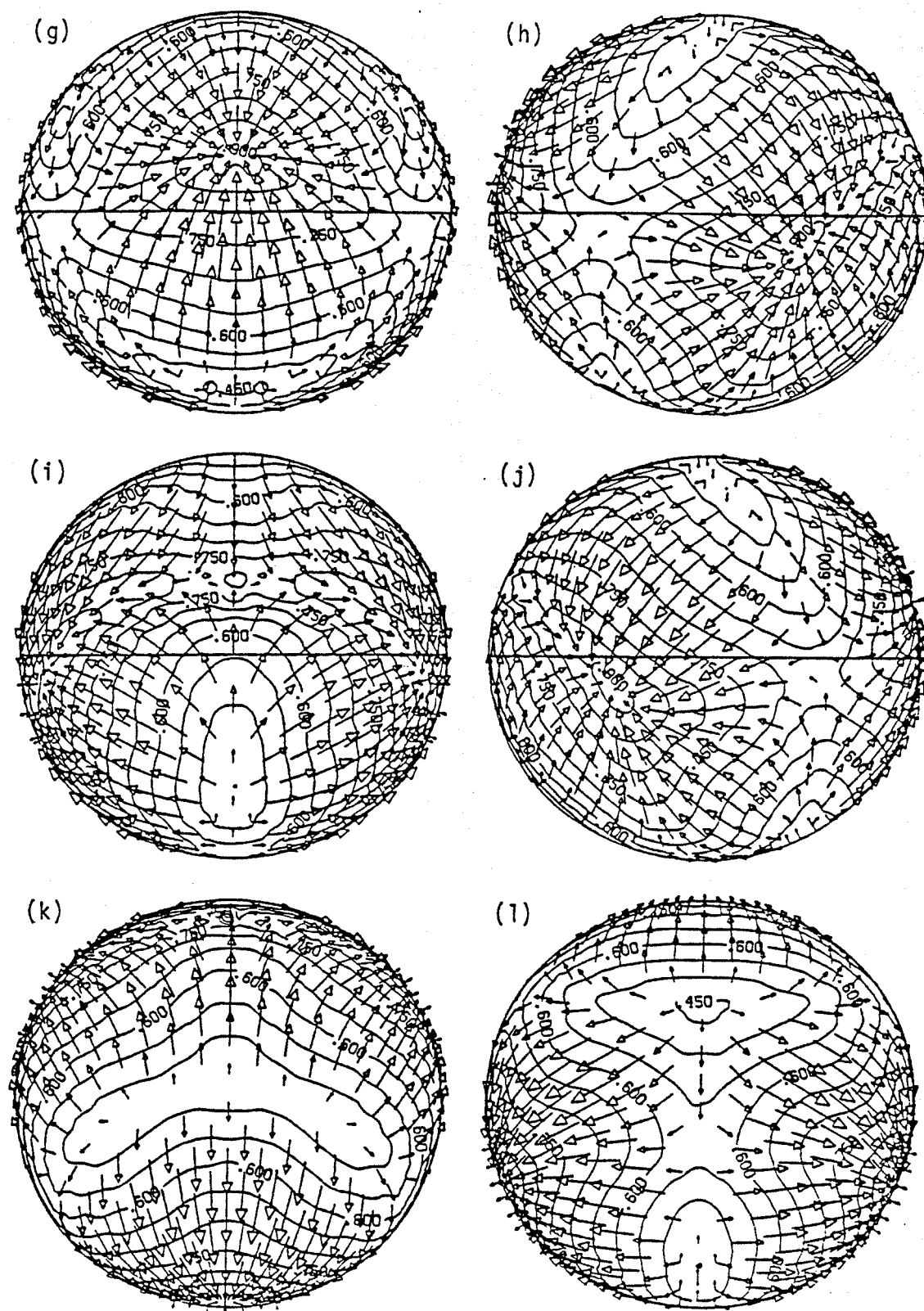


Figure 7.17. Convection solution for spherical shell, radius ratio 0.50, Rayleigh number 25,000, 75% internal heating, with gravitational acceleration increasing linearly with radius and initialized with solution of Figure 7.16. Velocity and temperature fields are displayed in (a)-(l). Orientations and radial positions of views are identical to those of Figure 7.2. Views (a)-(f) are at a normalized radial position of 0.981 and have a maximum velocity of 98.4. Views (g)-(l) are at a normalized radius of 0.519 and have a maximum velocity of 166.9.

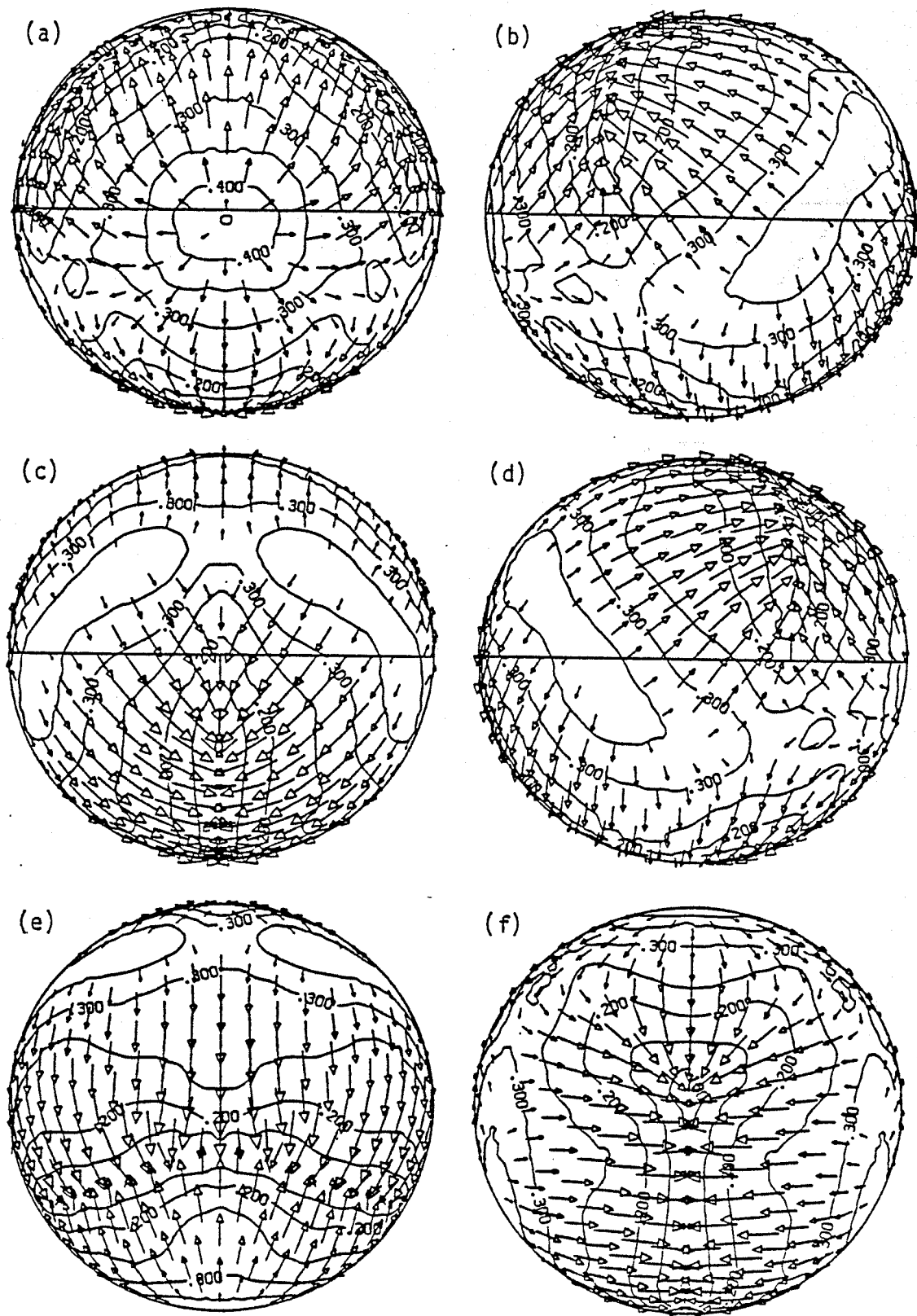


Figure 7.17

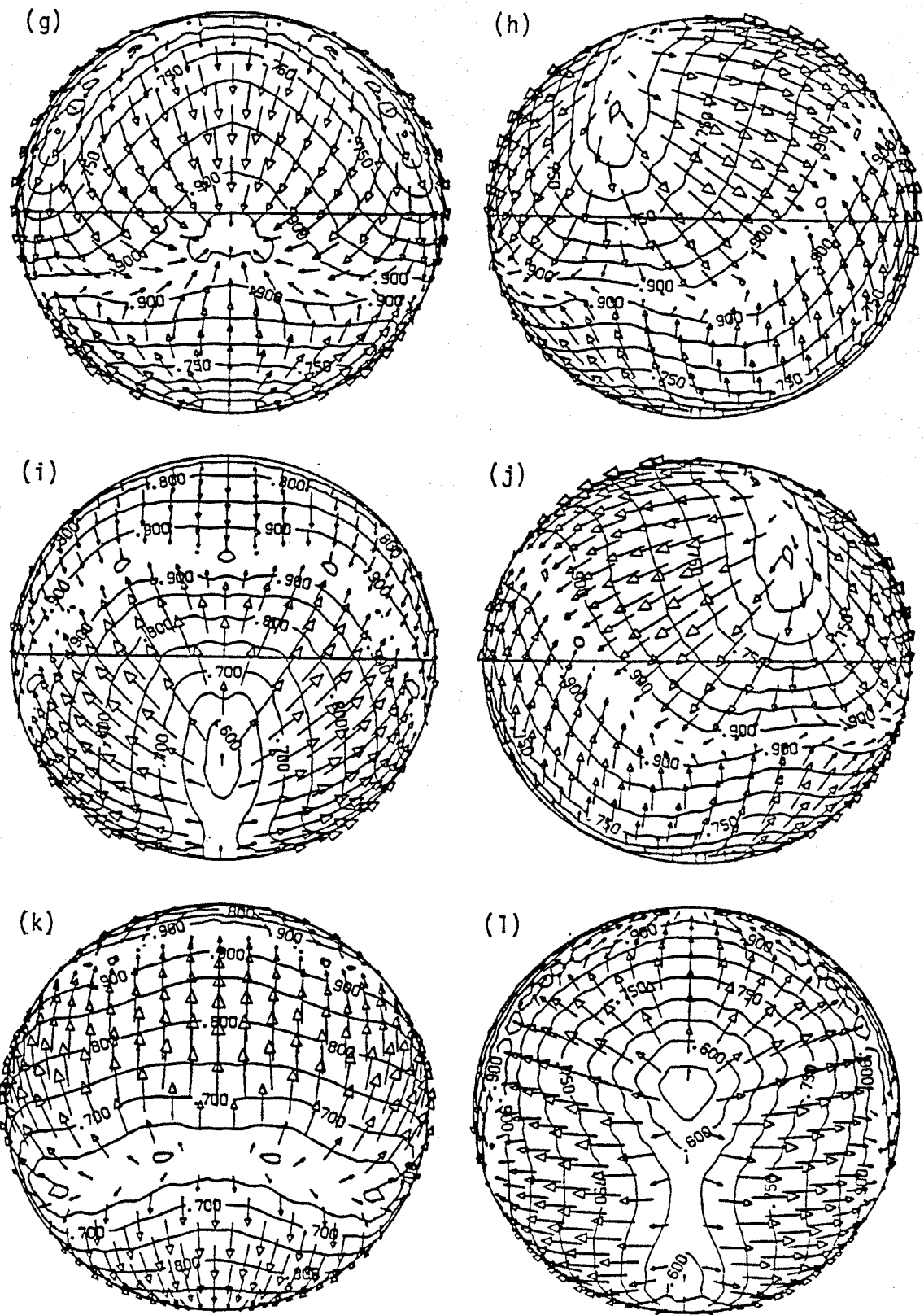


Figure 7.17

Figure 7.18. Spherically averaged radial temperature profiles for convection in spherical shell, radius ratio 0.50, Rayleigh number 25,000, with gravitational acceleration increasing linearly with radius: (a) 25% internal heating, (b) 50% internal heating, (c) 75% internal heating.

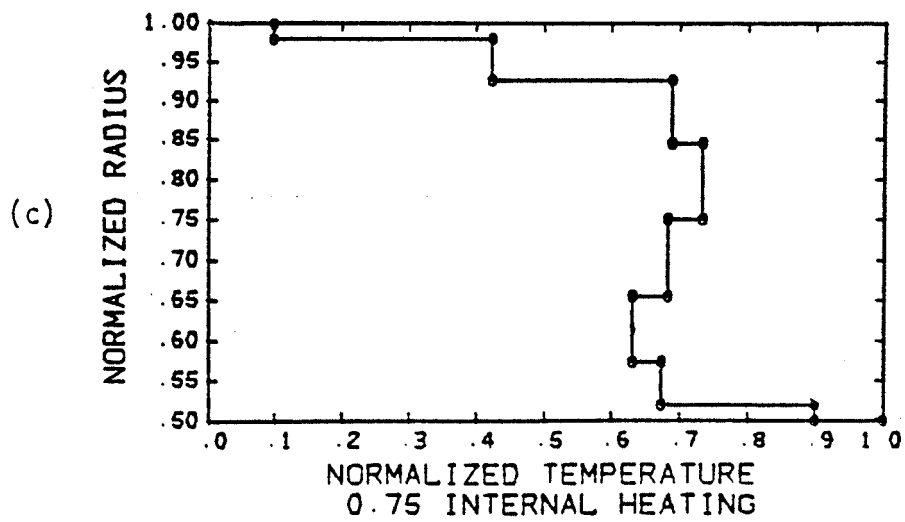
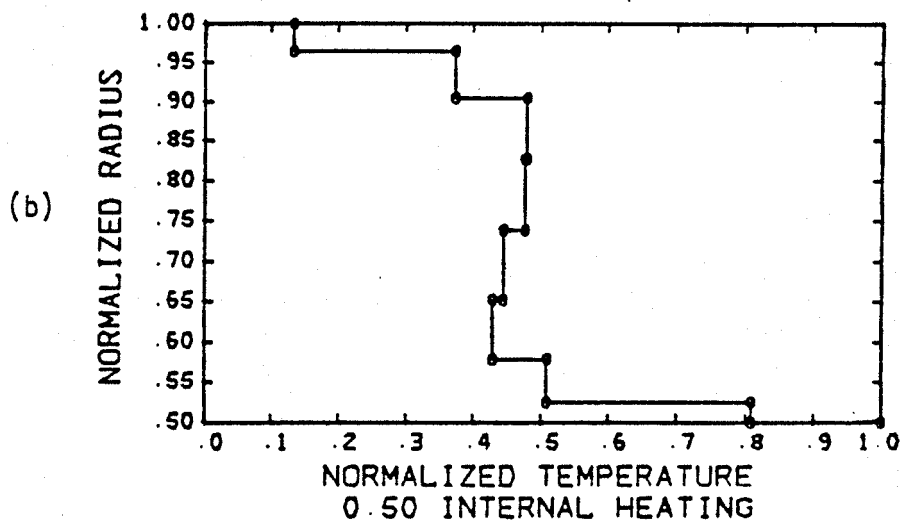
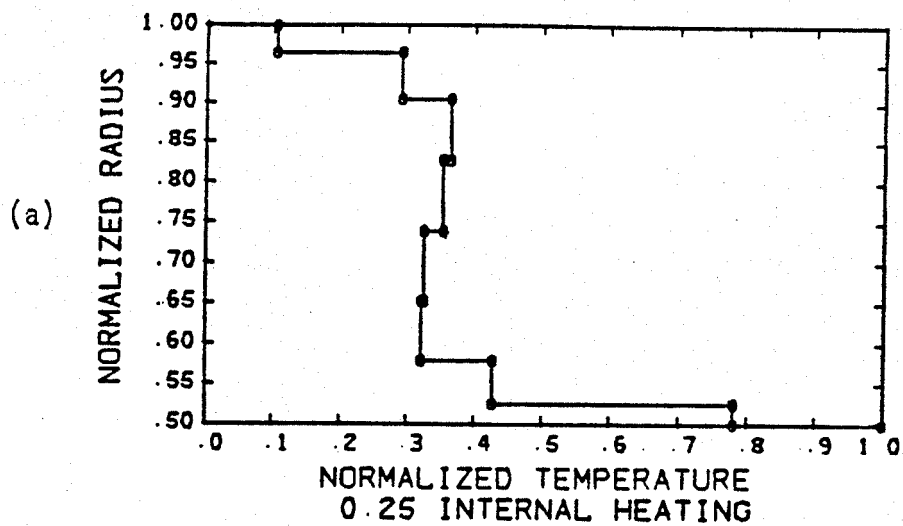


Figure 7.18

Figure 7.19. Spherically averaged radial and tangential velocity profiles for convection in spherical shell, radius ratio 0.50, Rayleigh number 25,000, with gravitational acceleration increasing linearly with radius: (a) 25% internal heating, (b) 50% internal heating, (c) 75% internal heating.

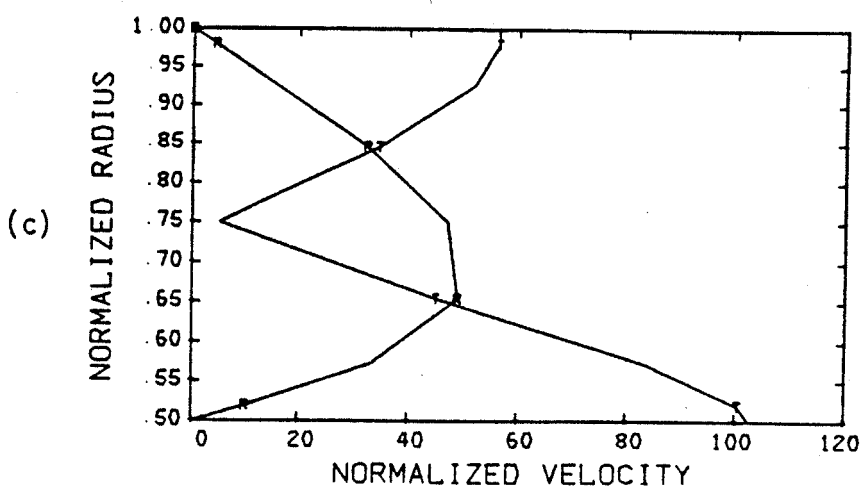
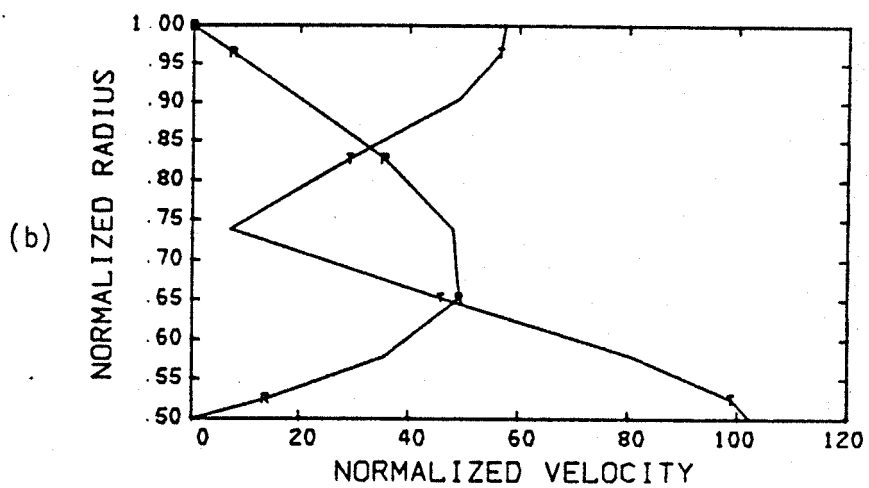
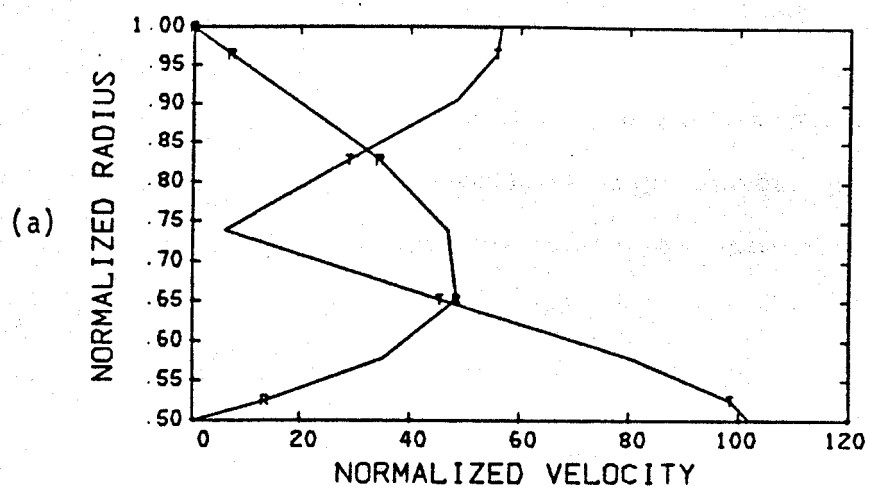


Figure 7.19

8. APPLICATION TO THE EARTH'S MANTLE

Upon specification of the shell radius ratio, mode of heating, radial variation of gravity, bulk modulus, thermal expansivity, and the initial conditions, the non-dimensional Rayleigh number completes the description of the convection problem, given the approximations listed at the beginning of the previous chapter. Applying methods used in the last chapter to the problem of thermal convection in the earth's mantle therefore involves relatively few changes.

In the three experiments to be described in this chapter, a different radius ratio, 0.547 instead of 0.50, and a constant gravitational acceleration, in contrast to the linearly increasing gravity with radius of the last chapter, are used. The new radius ratio is obtained by taking the mean radius of the earth (stripped of its oceans), 6368 km, as the outer radius and the PEM value for the core-mantle boundary, 3485 km, as the inner radius. The assumption of uniform gravitational acceleration through the mantle is a good approximation, as can be verified by referring to any of the standard earth models. This approximate uniformity is a consequence of the high density of the core relative to the mantle and to the density variation within the mantle itself. The mode of heating for these experiments is approximately 50 percent heating from below and 50 percent from within. The nominal values for bulk modulus and thermal expansivity used in the last chapter are also used here. The difference among the experiments is the initial conditions.

8.1 MANTLE CONVECTION WITH $L = 3$ INITIAL TEMPERATURES

This experiment uses the preferred solution of Section 7.1 as its initial condition. Model parameters match quite closely those actually used in Chapter 7 and are listed in Table 8.1. Cases were run at Rayleigh numbers, defined by equation (7.1), of 25,000 and 100,000.

Figures 8.1 and 8.2 show the solutions obtained. The solution of Figure 8.1 closely matches that of Figure 7.16, which has the same nominal Rayleigh number and fraction of internal heating. The difference is that the Figure 8.1 case has a slightly higher radius ratio and constant gravitational acceleration which gives it an effective Rayleigh number about 30% higher. In the patterns of Figures 8.1 and 8.2 the downwelling region which separated the two large cells at 180° longitude in heated from below cases has disappeared near 30° latitude, and the two large cells have essentially combined to form a single giant dumbbell-shaped cell. There is little change in the pattern the Rayleigh number is increased from 25,000 to 100,000. The radial temperature profiles are almost identical except for a reduced boundary layer thickness at $R = 100,000$.

For these two cases, the heat flow increases from 22.0 mW/m^2 to 30.2 mW/m^2 as the Rayleigh number is increased by the factor of four. If the Nusselt number varies according to $R^{2/3}$ as found for heating strictly from below in Chapter 7, the heat flow for the $R = 100,000$ case should have been 32.7 mW/m^2 . The 8 percent discrepancy is mostly a consequence of underresolution of the $n = 8$ grid at this Rayleigh number. However, given that the $n = 16$ grid is on the order of 25 times more costly and that little difference was observed in

the resulting pattern at higher resolution for the $R = 100,000$ case in Chapter 7, it is deemed useful to perform preliminary exploration at these high Rayleigh numbers using the coarser grid.

Table 8.1. Model parameters for mantle convection experiments for Rayleigh number of 25,000.

| | | |
|---|------------------------|-------------------|
| Outer radius of mantle | 6.368×10^6 | m |
| Inner radius of mantle | 3.485×10^6 | m |
| Mean density | 4.500×10^3 | kg/m ³ |
| Dynamic shear viscosity | 4.519×10^{22} | kg/m/s |
| Bulk modulus | 2.500×10^{10} | Pa |
| Volume coefficient of thermal expansion | 2.500×10^{-7} | K ⁻¹ |
| Thermal conductivity | 4.000 | W/m/K |
| Specific heat | 1.000×10^3 | J/kg/K |
| Gravitational acceleration | 10.0 | m/s |
| Volumetric radiogenic heat production | 6.000×10^{-9} | W/m ³ |
| Outer boundary temperature | 275.0 | K |
| Inner boundary temperature | 4000.0 | K |

Note: R = 100,000 case used a viscosity of 1.130×10^{22} kg/m/s and a heat production of 8.400×10^{-9} W/m.
R = 1,000,000 case used a viscosity of 1.130×10^{21} kg/m/s and a heat production of 1.600×10^{-8} W/m.

Figure 8.1. Convection solution for spherical shell, representing the earth's mantle, radius ratio 0.547, Rayleigh number 25,000, 48% internal heating, constant amplitude gravitational acceleration, initialized with pattern of Figure 7.2. Velocity and temperature fields are displayed in (a)-(l). Orientations of views are identical to those of Figure 7.2. Radial position for views (a)-(f) is 6170 km, and maximum velocity is 1.01 mm/yr. Radial position for views (g)-(l) is 3635 km, and maximum velocity is 1.81 mm/yr. Temperature contours in (a)-(l) are normalized to the inner boundary temperature of 4000 K. Temperature of outer boundary is 275 K. (m) shows the spherically averaged radial and tangential velocity profiles and (n) the spherically averaged radial temperature profile. The internally generated heat and the fixed temperature imposed at the inner boundary account for the character of the conductive profile in (n). (o)-(r) are time history plots, respectively, of RMS nodal velocity normalized by κ/d , where $\kappa = 8.89 \times 10^{-8} \text{ m}^2/\text{s}$ and $d = 2883 \text{ km}$; mean shell temperature normalized such that the outer boundary has temperature zero and the inner boundary one; heat flow through the outer boundary normalized by the purely conductive state heat flow in the absence of internal heating; and the heat flow through the inner boundary similarly normalized. Time in these plots is normalized by d^2/κ .

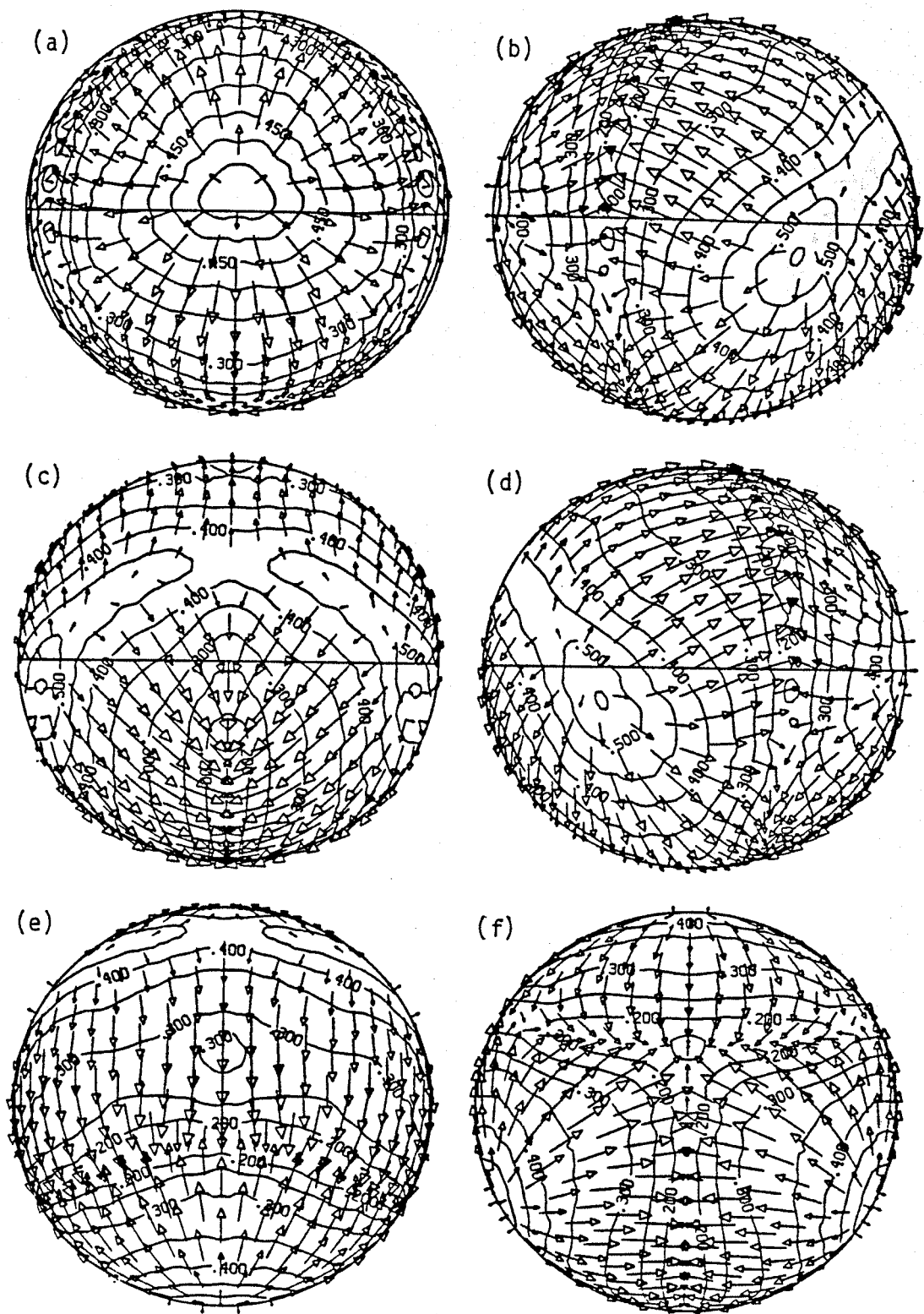


Figure 8.1

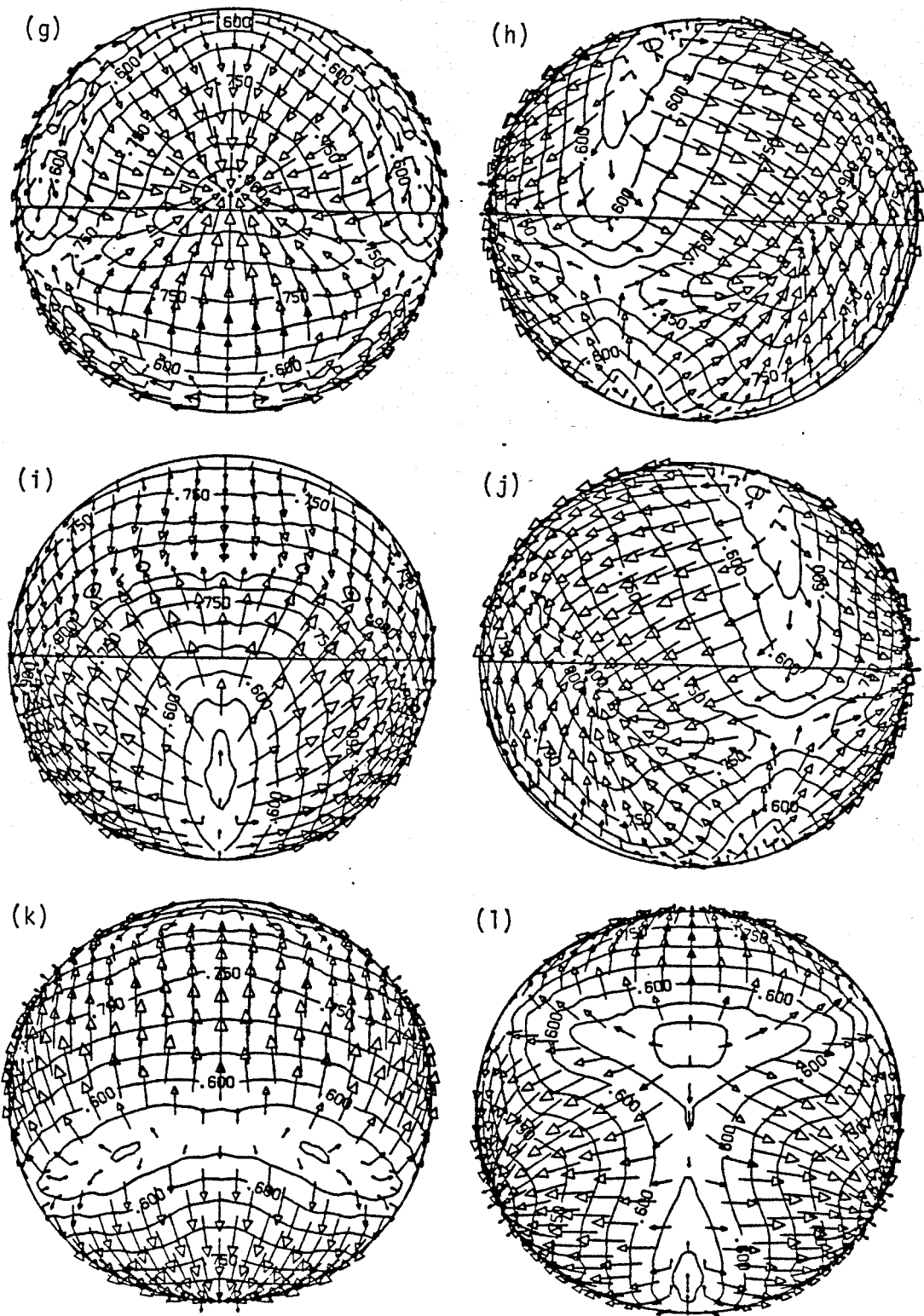


Figure 8.1

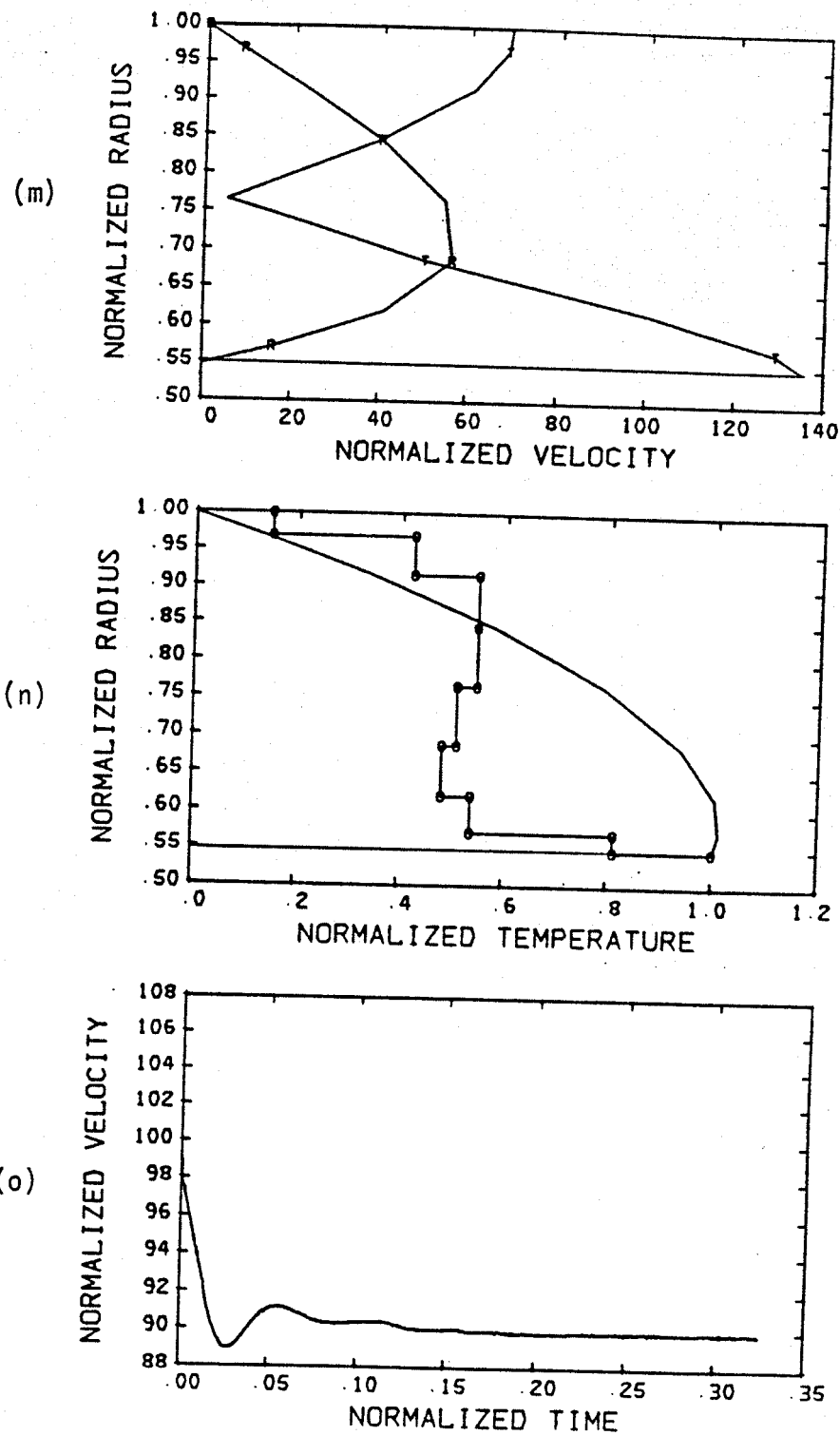


Figure 8.1

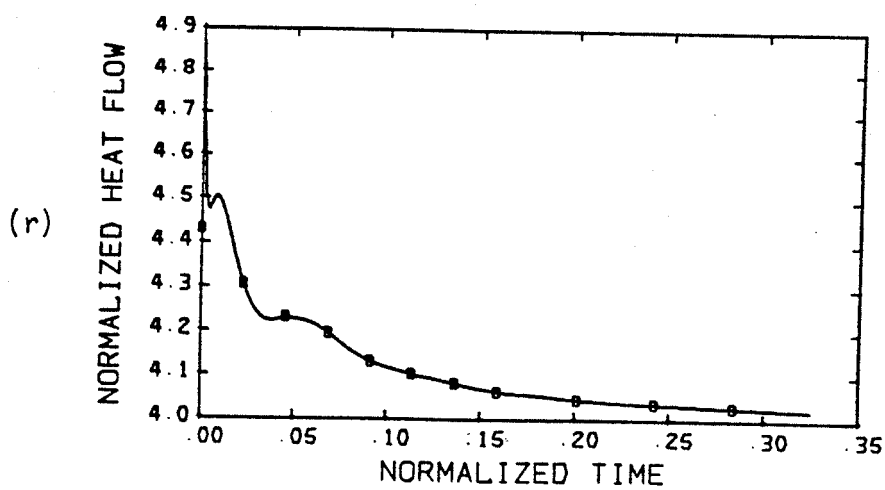
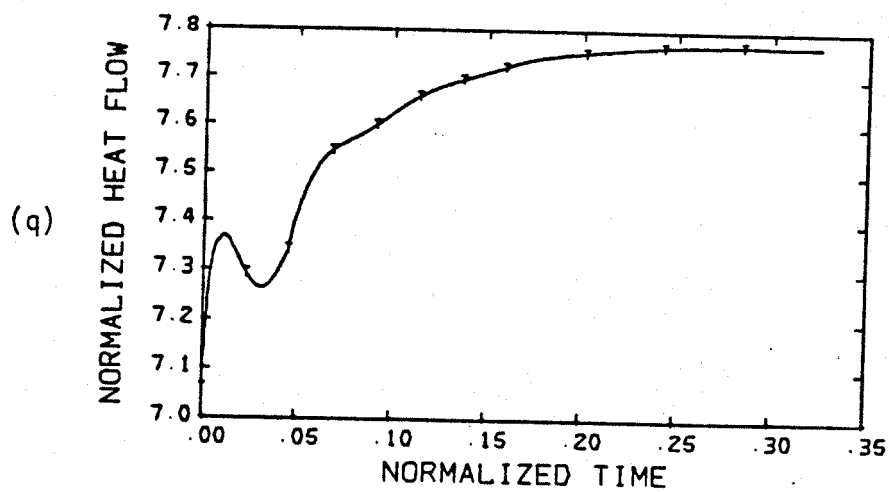
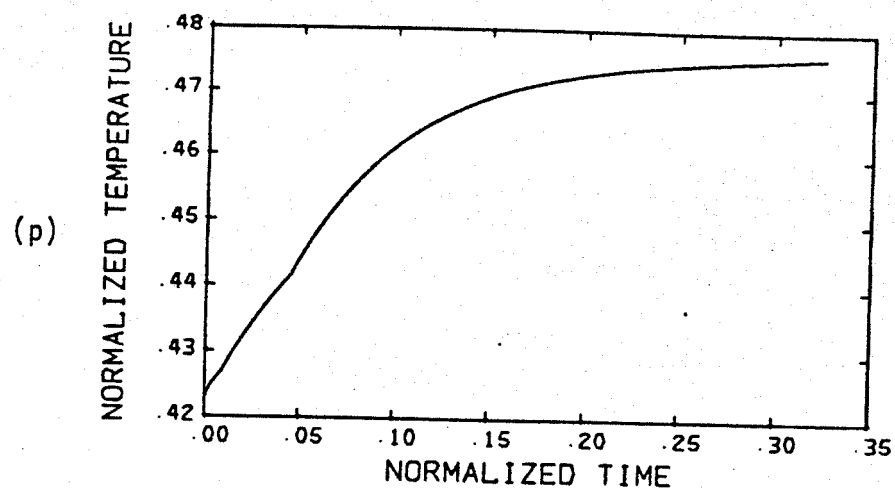


Figure 8.1

Figure 8.2. Convection solution for spherical shell, representing the earth's mantle, radius ratio 0.547, Rayleigh number 100,000, 48% internal heating, constant amplitude gravitational acceleration, initialized with solution of Figure 8.1. Velocity and temperature fields are displayed in (a)-(l). Orientations of views are identical to those of Figure 7.2. Radial position for views (a)-(f) is 6258 km, and maximum velocity is 2.77 mm/yr. Radial position for views (g)-(l) is 3595 km, and maximum velocity is 5.03 mm/yr. Temperature contours in (a)-(l) are normalized to the inner boundary temperature of 4000 K. Temperature of outer boundary is 275 K. (m)-(r) have same significance and normalization as in Figure 8.1.

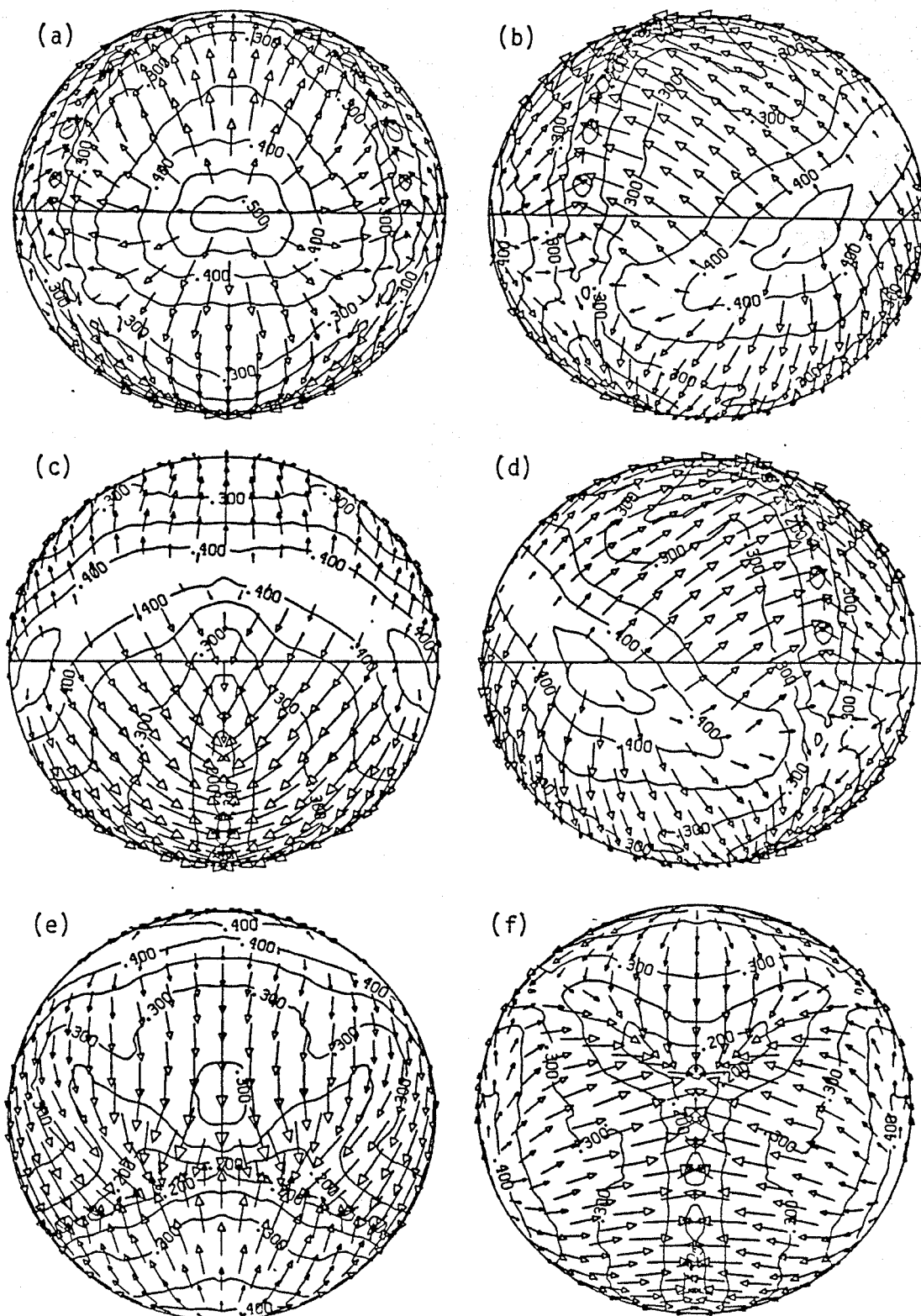


Figure 8.2

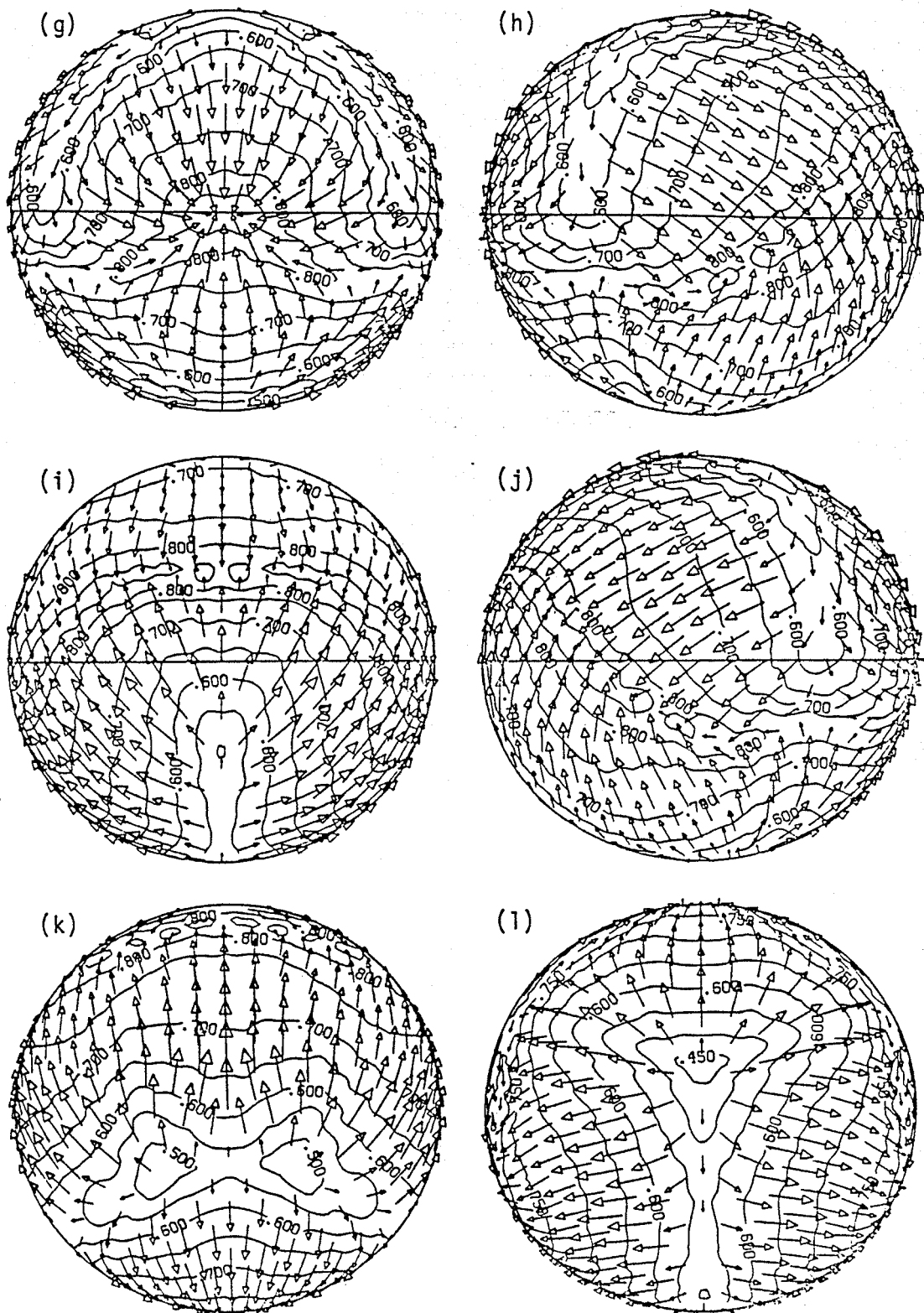
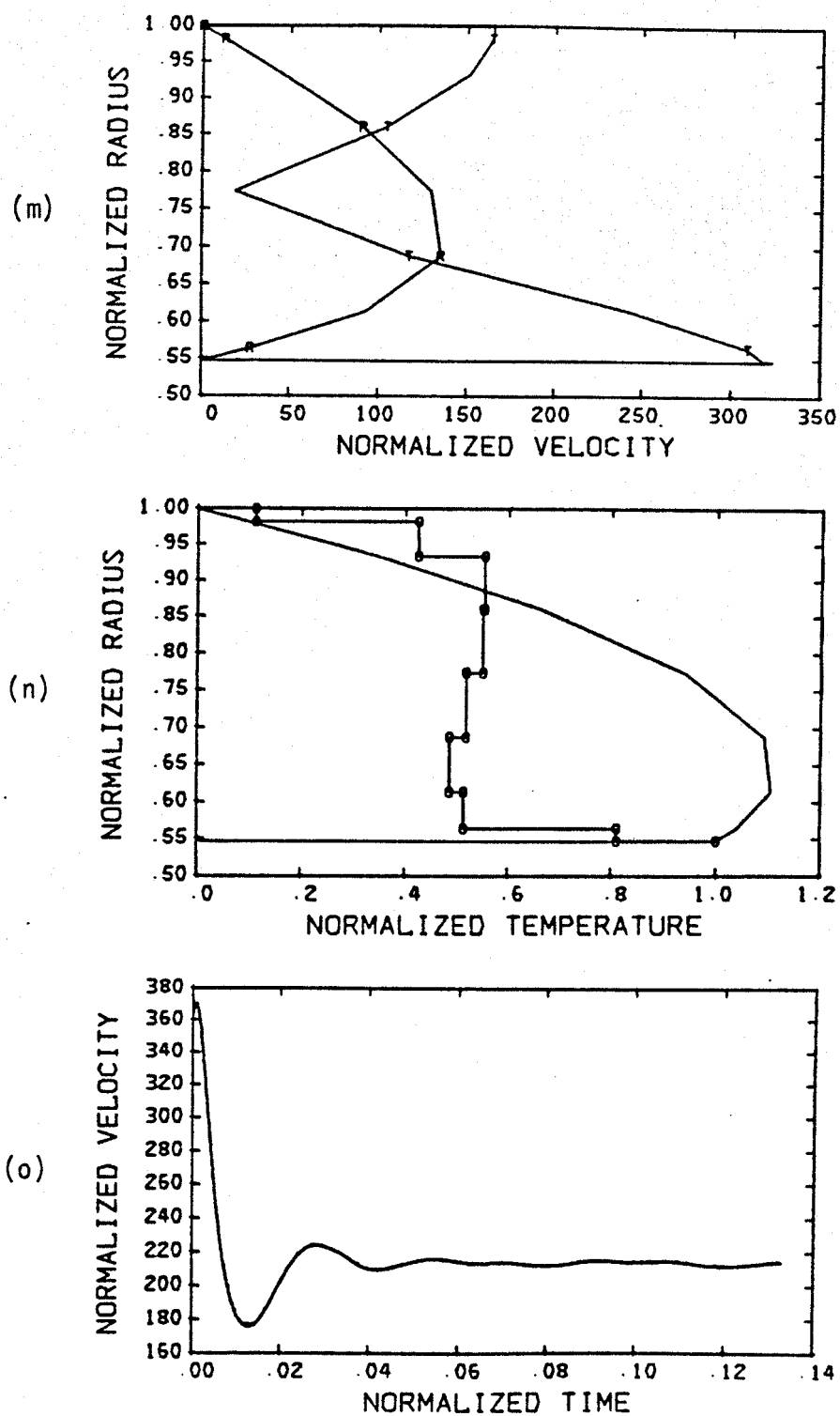


Figure 8.2



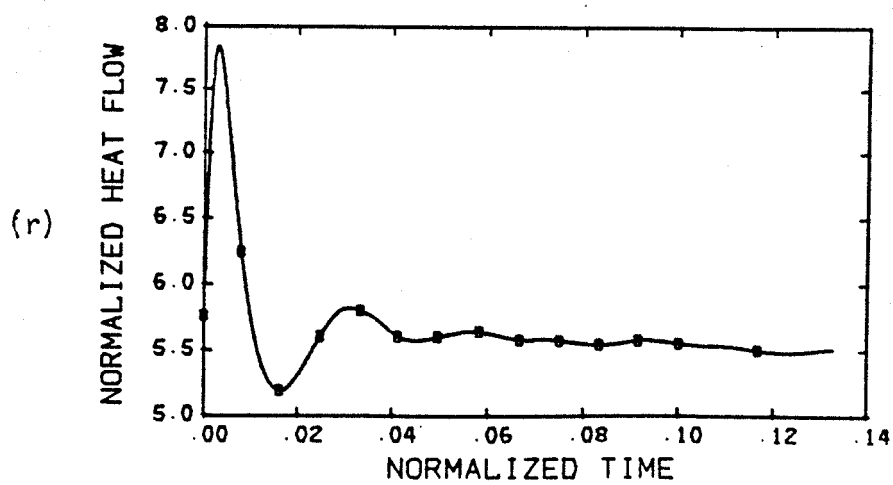
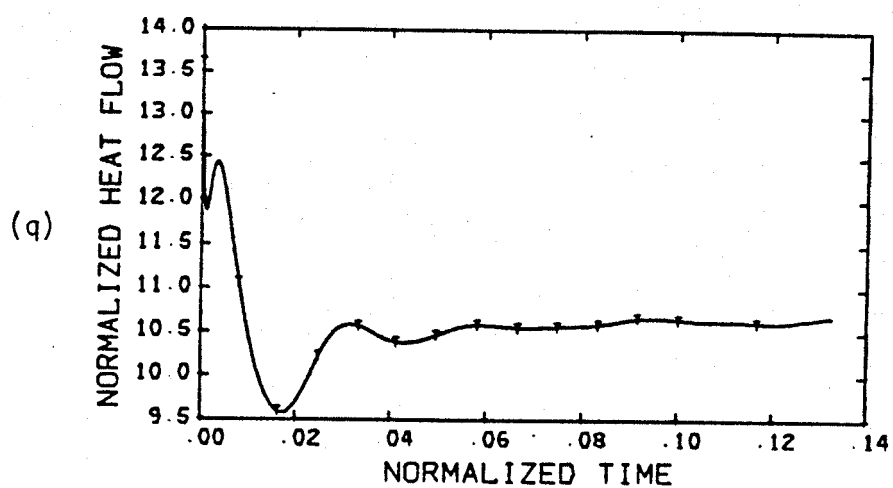
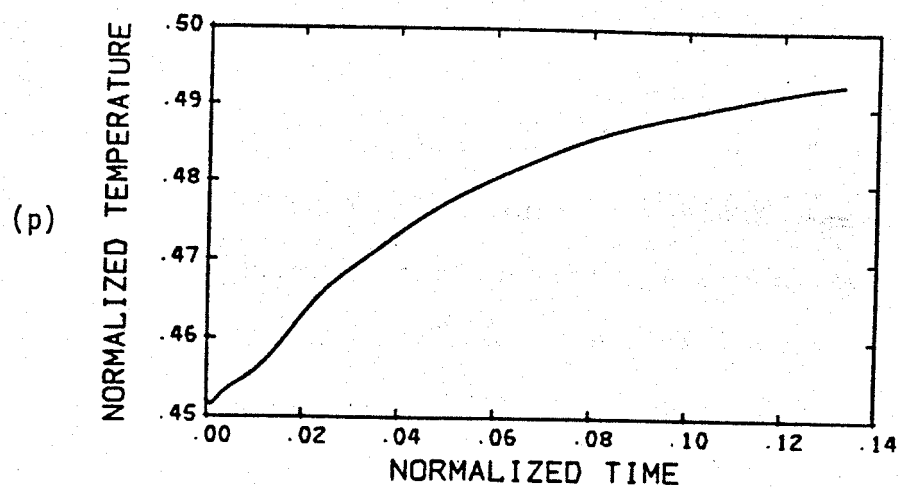


Figure 8.2

8.2 MANTLE CONVECTION WITH RANDOM INITIAL CONDITIONS

This experiment is identical to that of the previous section except that, instead of the preferred pattern of Section 7.1 as the initial condition, a random initial temperature distribution was used. The solutions after approximately 3.5 convective overturn times are shown in Figure 8.3 for the $R = 25,000$ case and Figure 8.4 for the $R = 100,000$ case. The fact that the RMS velocity is still increasing slightly at the end of the runs indicates that the solutions have not yet reached their steady configurations. Both solutions display three well-defined cells and qualitatively resemble the solutions of the preceding section. The heat flows of 22.2 mW/m^2 and 30.3 mW/m^2 , respectively, agree closely with the values of the last section. At the outer boundary, the solutions are characterized by broad areas of divergent upwelling flow and more localized and intense linear regions of downwelling flow.

Figure 8.3. Convection solution for spherical shell, representing the earth's mantle, radius ratio 0.547, Rayleigh number 25,000, 48% internal heating, constant amplitude gravitational acceleration, initialized with random initial temperatures. Velocity and temperature fields are displayed in (a)-(l). Orientations and radial positions of views and normalization of temperature contours are identical to views (a)-(l) of Figure 8.1. Maximum velocity for views (a)-(f) is 1.03 mm/yr and for views (g)-(l) is 1.81 mm/yr. (m)-(r) have same significance and normalization as in Figure 8.1.

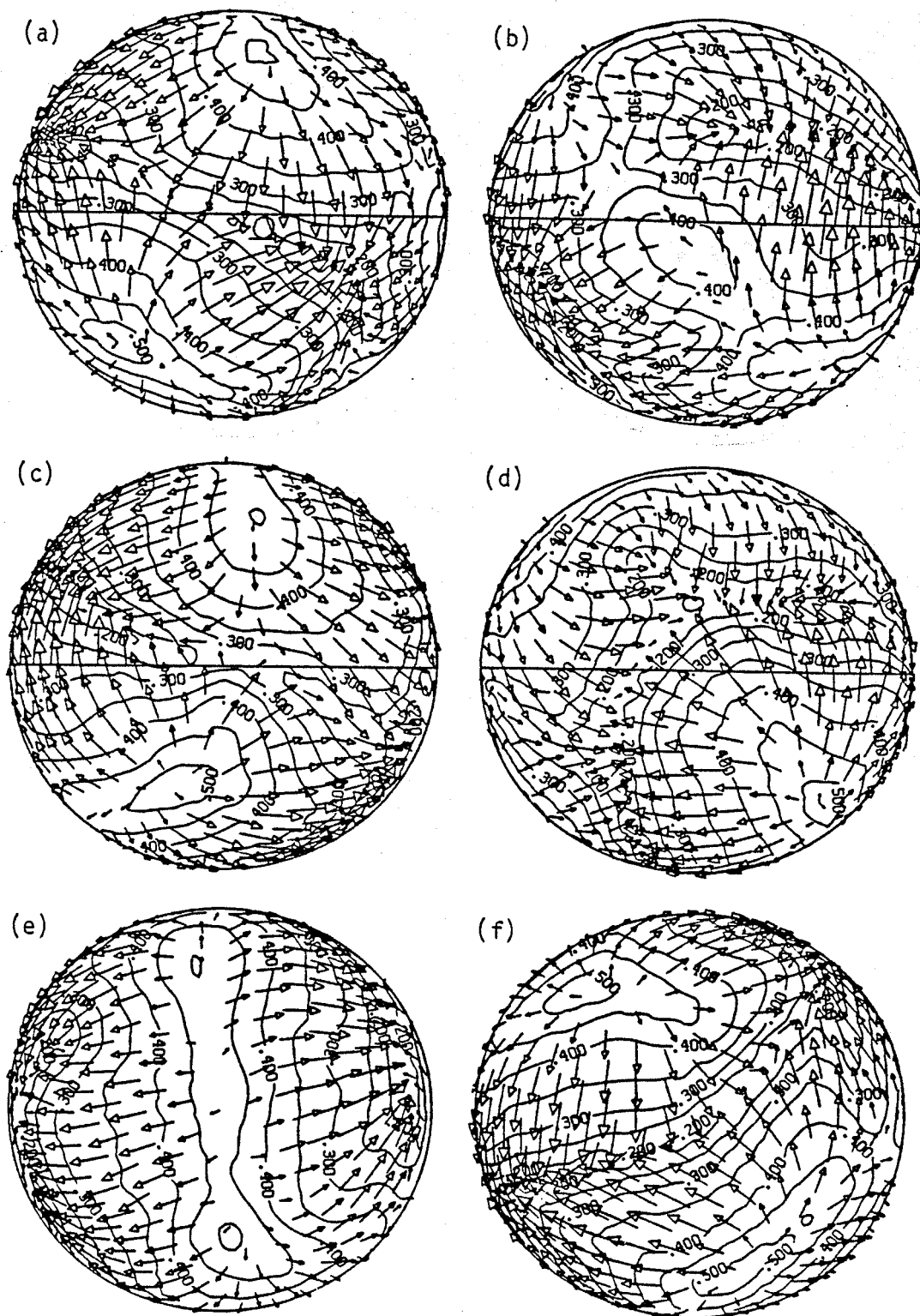


Figure 8.3

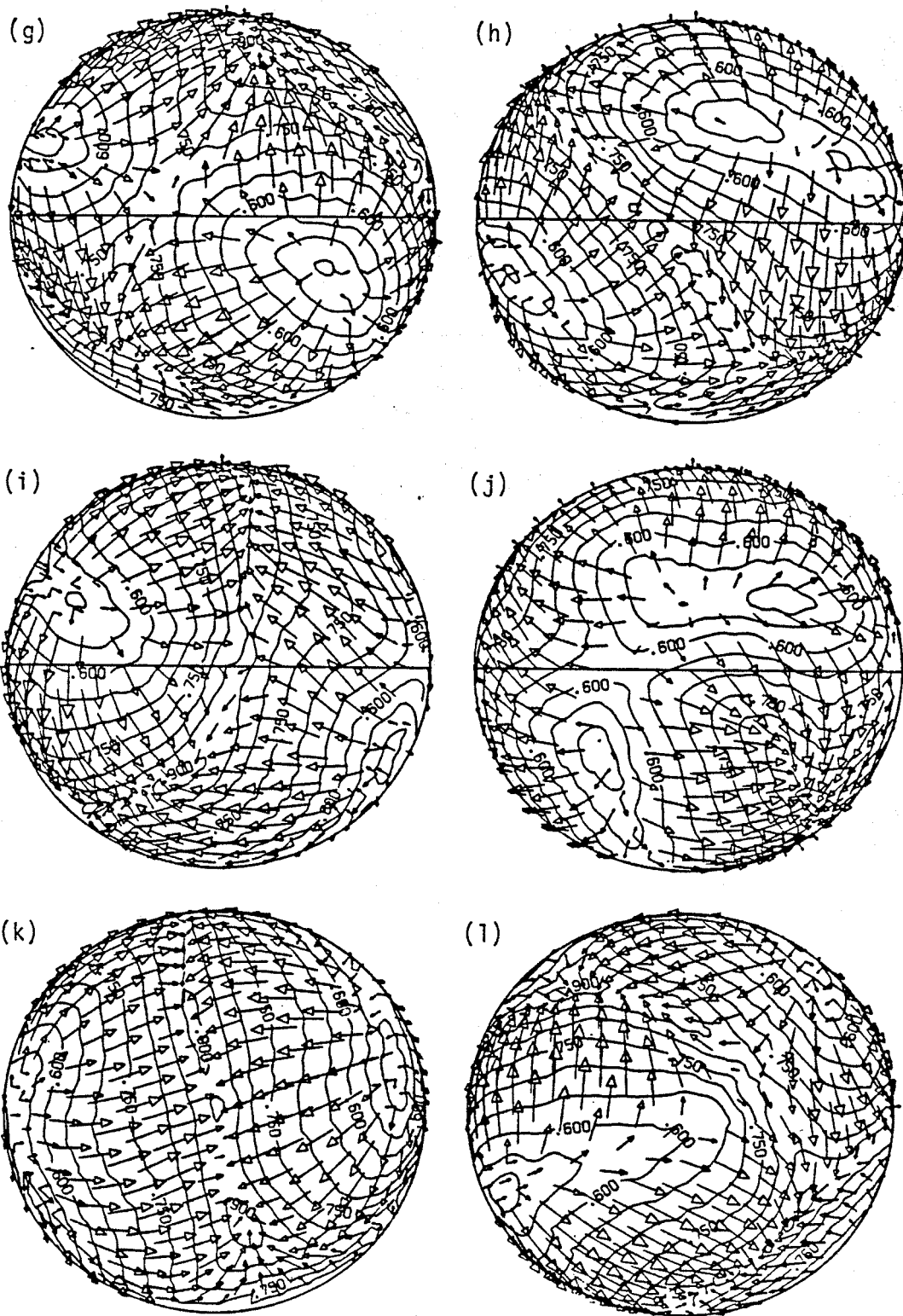


Figure 8.3

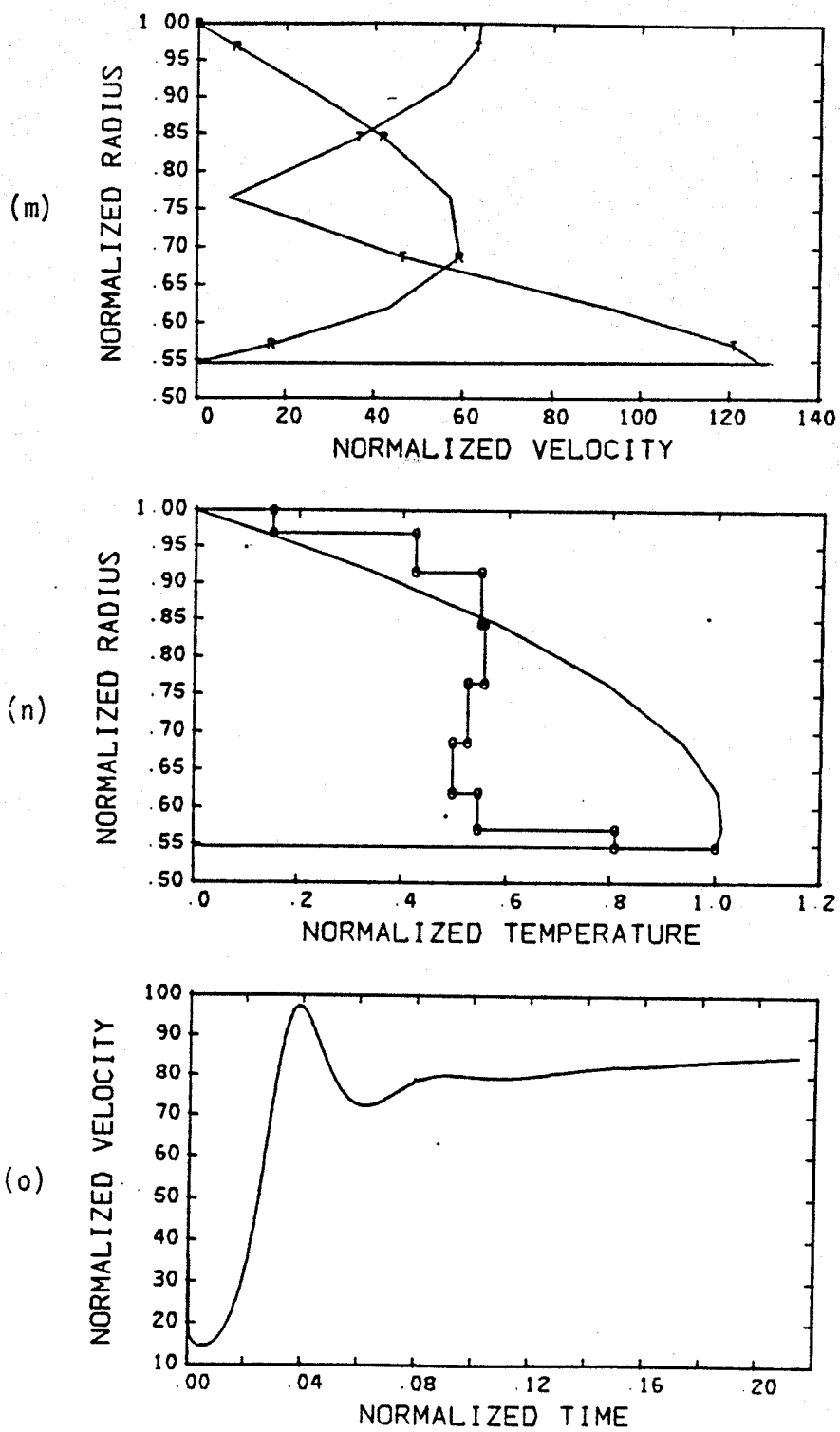


Figure 8.3

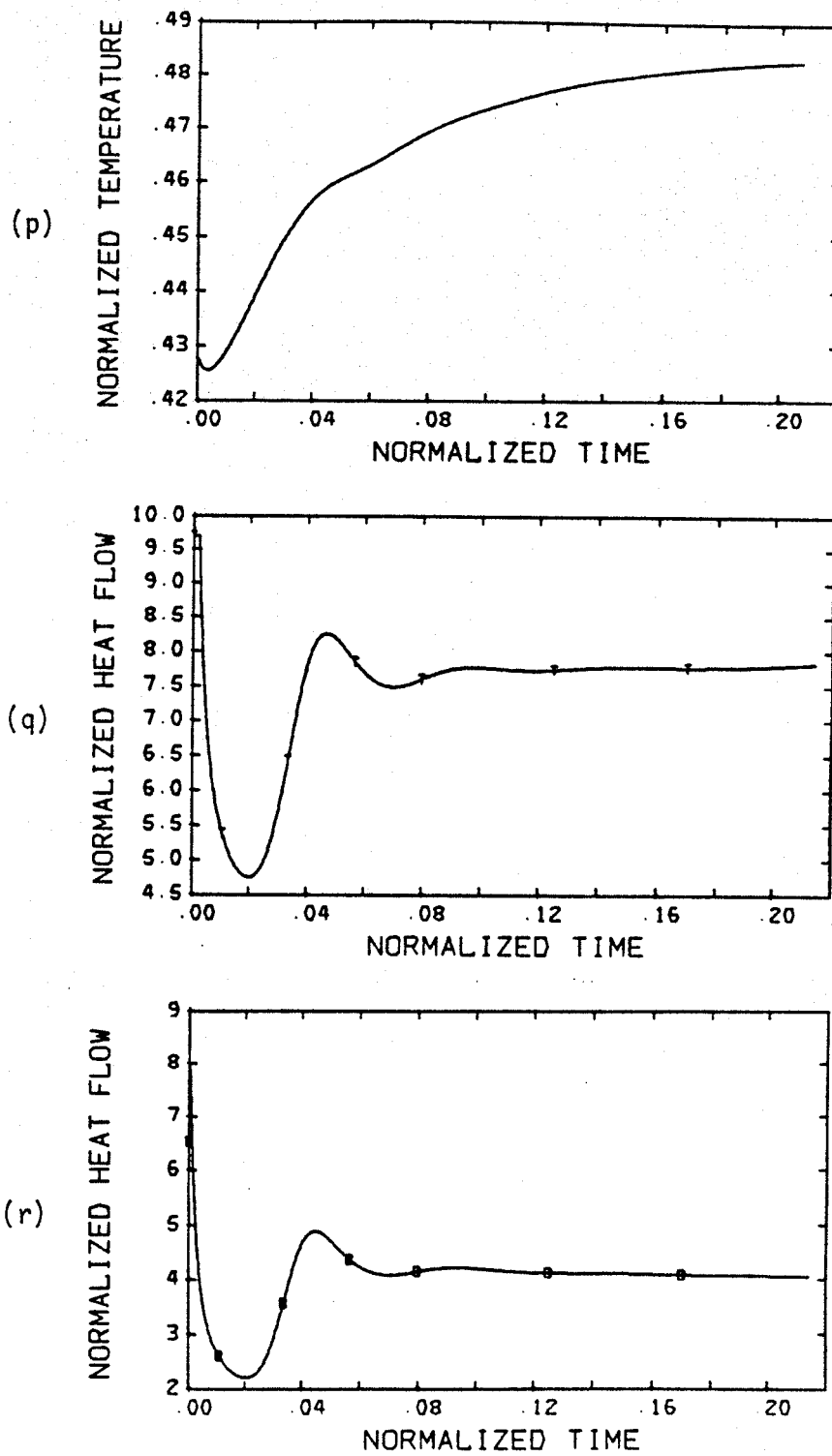


Figure 8.3

Figure 8.4. Convection solution for spherical shell, representing the earth's mantle, radius ratio 0.547, Rayleigh number 100,000, 48% internal heating, constant amplitude gravitational acceleration, initialized with random initial temperatures. Velocity and temperature fields are displayed in (a)-(l). Orientations and radial positions of views and normalization of temperature contours are identical to views (a)-(l) of Figure 8.2. Maximum velocity for views (a)-(f) is 3.00 mm/yr and for views (g)-(l) is 5.11 mm/yr. (m)-(r) have same significance and normalization as in Figure 8.1.

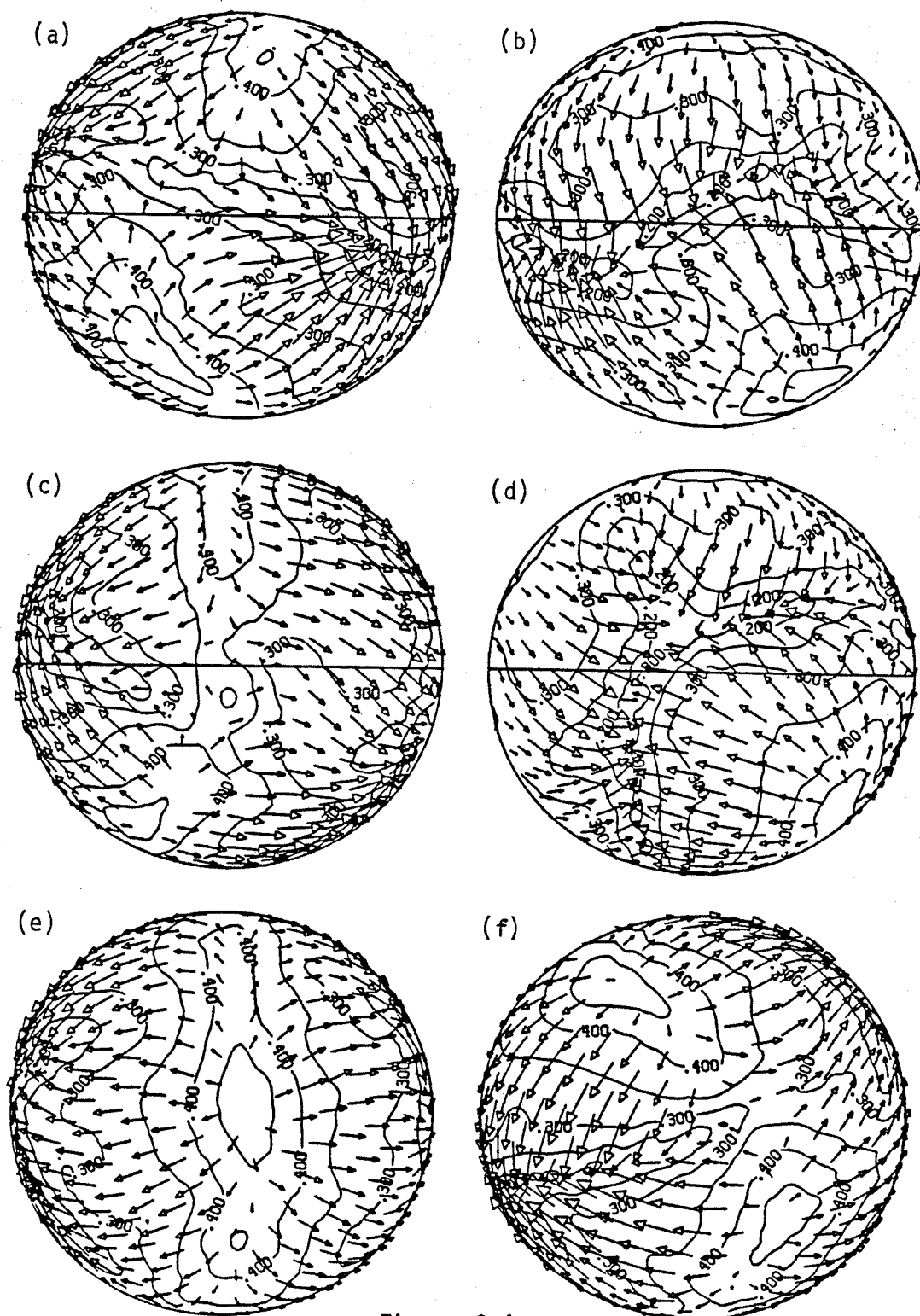


Figure 8.4

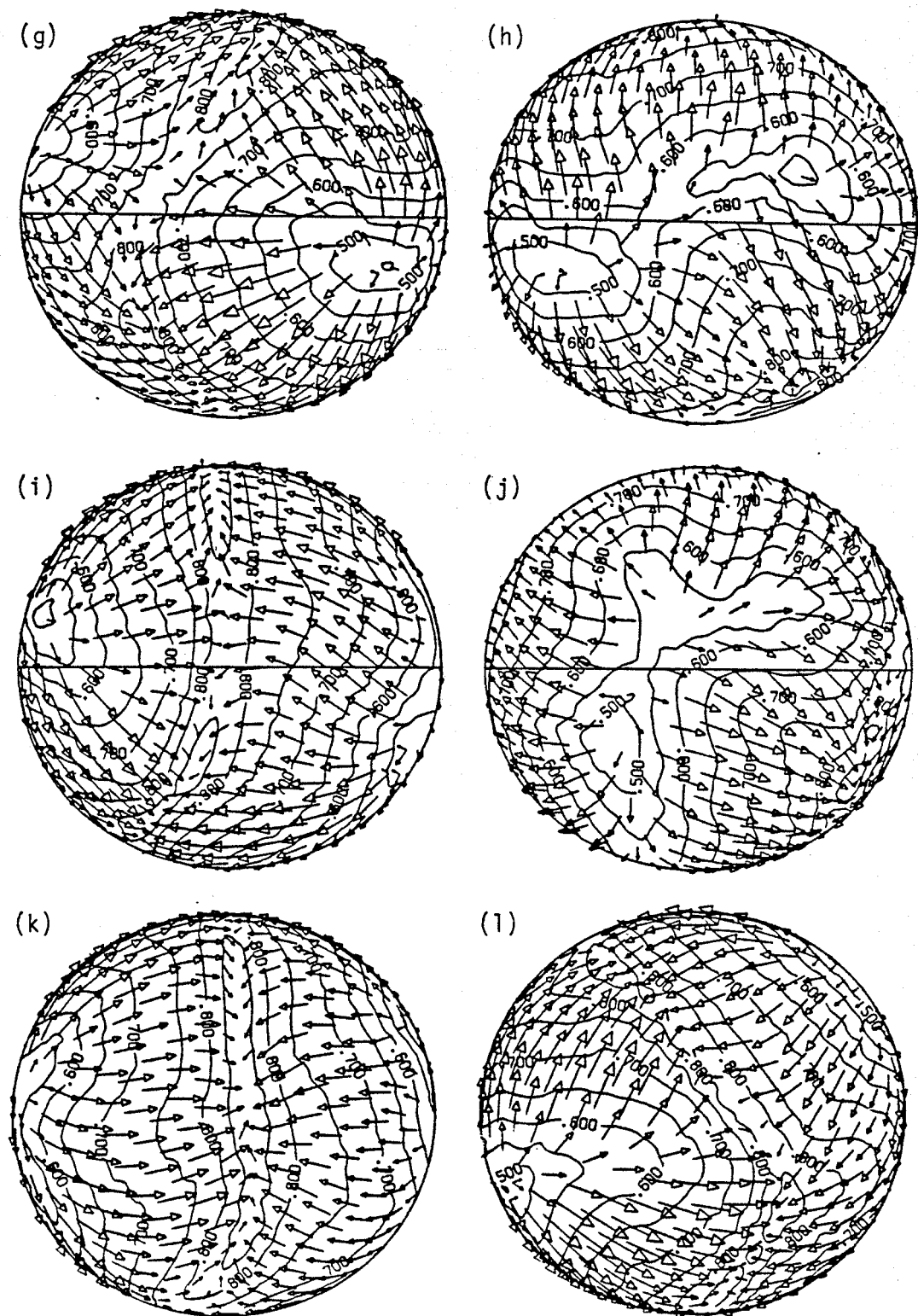


Figure 8.4

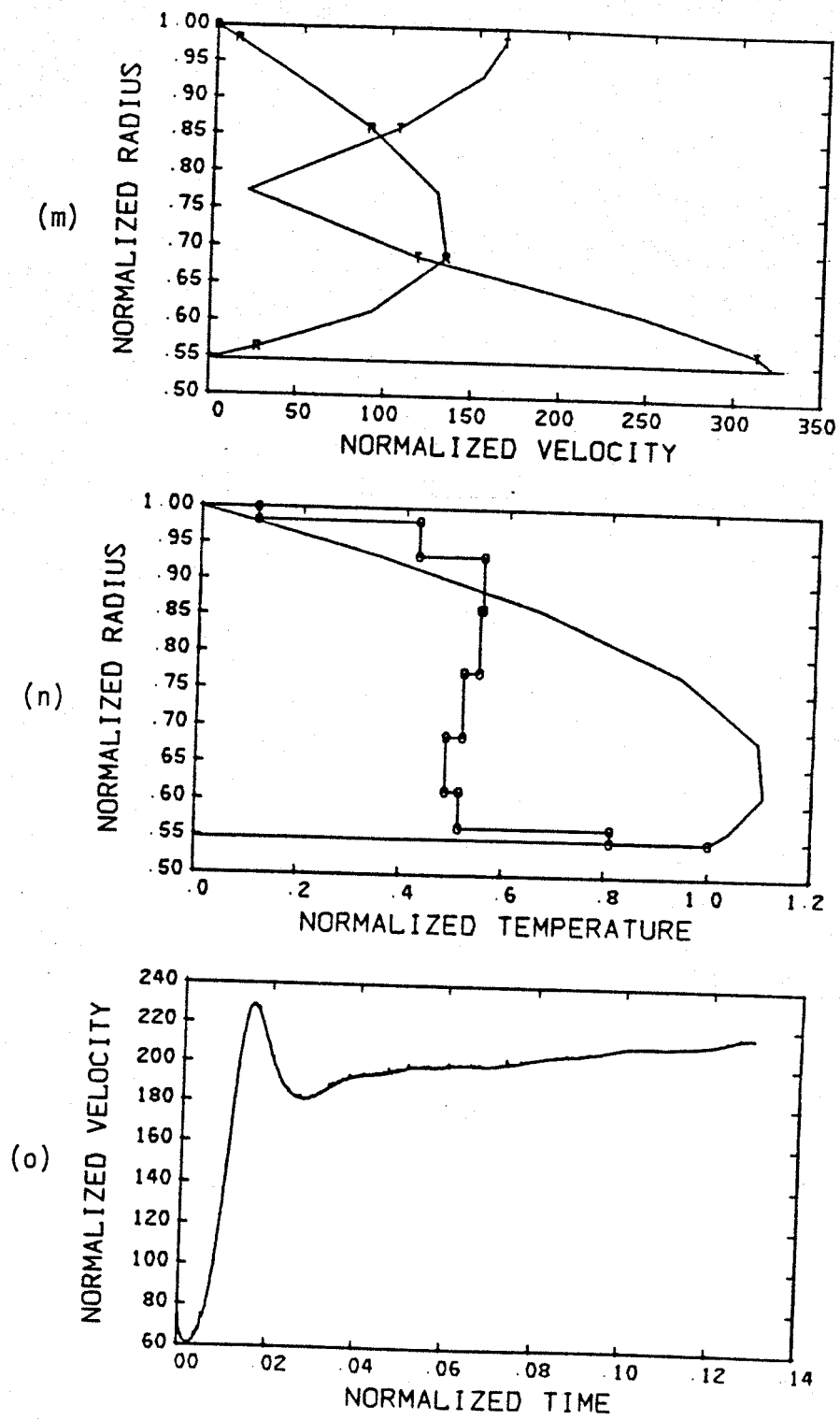


Figure 8.4

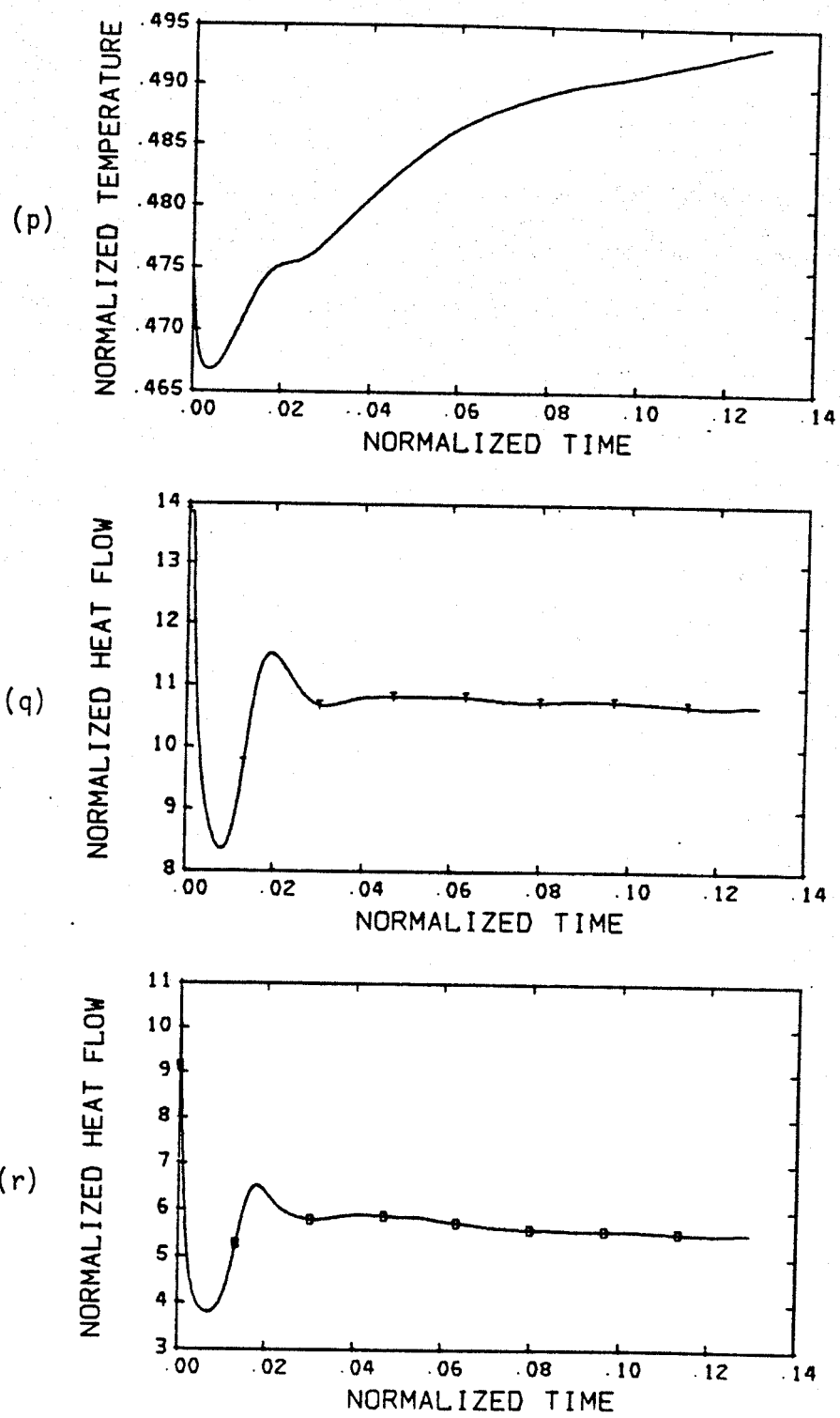


Figure 8.4

8.3 MANTLE CONVECTION WITH RIDGE/TRENCH DISTRIBUTION SPECIFYING INITIAL TEMPERATURES

This experiment is similar to that of the previous two sections except that a temperature distribution warmer beneath present mid-ocean ridges and cooler adjacent to subducting trenches is used as the initial condition. Cases were run with $n = 8$ grids at $R = 25,000$ and $R = 100,000$ and with $n = 16$ grids at $R = 1,000,000$.

Figure 8.5 shows the temperature field for the $R = 25,000$ case early in its time history and reveals the character of the initial temperature distribution. Figures 8.6-8.9 show the solution at approximately 0.08, 0.75, 2.0, and 3.3 overturn times. A number of general observations can be made. One is the good correlation between the velocity field at the outer boundary and present plate motions, although the agreement is better near the beginning than at the end of the run. The pattern is surprisingly stable, with its basic character persisting throughout the three convective overturns. Changes that do occur include migration of the Indian Ocean upwelling region northward, a similar northward extension of the East Pacific upwelling region, and a southward extension of the downwelling region beneath Africa across the South Atlantic. At the final time, the mean surface velocity is 0.60 mm/yr and the mean surface heat flow 22.3 mW/m².

Although there is no detailed correspondence between this pattern and the $R = 25,000$ solutions of the preceding two sections, the spatial frequencies, mean temperatures, global heat flows, and spherically

averaged radial temperature profiles are quite similar. This suggests that the relative stability observed during the brief time the solution was followed would persist and that convergence to an ideal preferred pattern would require several more convective overturns.

Figures 8.10-8.14 show a similar sequence of snapshots for the solution at $R = 100,000$. These snapshots are taken at approximately 0.1, 0.9, 2.3, 3.0, and 4.0 convective overturn times. The changes which occur during this interval correspond closely with those of the $R = 25,000$ case. At the end of the run there is essentially a single connected region of upwelling, extending from what is presently western Asia, south through the Indian Ocean, across the southern and eastern Pacific, northeastward through western and northern North America, and finally southward through the Atlantic. Downwelling is thereby divided into two identifiable regions, one centered in the far western Pacific and the other forming a horseshoe pattern beneath eastern Europe and Africa, across the south Atlantic, northward beneath South America, and into the Caribbean. This case had a RMS surface velocity of 1.58 mm/yr and a mean surface heat flow of 30.4 mW/m².

Values of $2.5 \times 10^{-5} \text{ K}^{-1}$ for α , 10 m/s^2 for g , $4.5 \times 10^3 \text{ kg/m}^3$ for ρ , 10^3 J/kg/K for c_p , $2 \times 10^3 \text{ K}$ for the superadiabatic ΔT , $2.88 \times 10^6 \text{ m}$ for the mantle thickness d , 4 W/m/K for k , and $3 \times 10^{21} \text{ kg/m/s}$ for μ yield an estimate for the Rayleigh number of the earth's mantle of 2.0×10^7 . Although the two cases just summarized suggest the single-layer pattern with upwelling flow correlated with current locations of sea-floor spreading is relatively stable, these

results should be interpreted with caution since the Rayleigh numbers are more than two orders of magnitude below that of the mantle.

The final two cases to be described have a Rayleigh number of 10^6 , a factor of 20 from the estimate for the earth. Both cases used $n = 16$ grids with 43554 nodes and 81920 cells. These cases were initialized with the $R = 100,000$ solution at 0.1 overturn time shown in Figure 8.10.

Figures 8.15 and 8.16 show the solution for a case which has thin layers of cells (28 km in thickness) at both inner and outer shell boundaries. Figure 8.15 displays the velocity and temperature distributions at approximately 0.9 overturn time. In plots (a)-(f) it is possible to identify seven upwelling plumes, three of which lie mostly in the northern hemisphere and four in the southern hemisphere. The solution after 1.8 overturn times in Figure 8.16 shows the plumes better established and the regions of downwelling organized into more clearly defined linear zones between plumes. The heat flow at this time is 65 mW/m^2 , and the RMS surface velocity is 5.8 mm/yr .

Two features in this solution distinguish it from what is actually observed for the earth. One is its high ratio of heat flow to surface velocity at the outer boundary. For the earth the heat flow is about 70 mW/m^2 while the RMS surface velocity is approximately 30 mm/yr . The second feature is the large amount of local variation in magnitude and direction in the velocity field. In contrast, the earth's tectonic plates tend to move as rigid units so that surface velocities show little local variation except at plate margins. Both departures from earth-like character in the numerical model are related to a lack of stiffness in the region near the outer boundary.

A simple means for obtaining a slightly improved representation for the earth's lithosphere without modifying any of the assumptions in the numerical method is to increase the thickness of the cells at the outer boundary. A second case, identical to the previous one except for its radial discretization, was run for approximately the same length of time. For this case the outermost layer of cells had a thickness of 150 instead of 28 km. The resulting solution is shown in Figures 8.17-8.21 at approximately 0.1, 0.7, 1.0, 1.4, and 1.7 convective overturn times, respectively. In Figure 8.17 much of the character of the initial condition is still discernable. After 0.7 overturn time (Figure 8.18), the plume-like style for the upwelling flow is appearing at the outer boundary. By 1.0 overturn time (Figure 8.19), seven upwelling plumes are clearly evident. Downwelling flow at the outer boundary is organized into linear zones between plumes. Snapshots at 1.4 and 1.7 overturn times (Figures 8.20 and 8.21) display relatively small changes in the pattern, changes which for the most part enhance the pattern's organization. Figure 8.21 (g)-(i) at a radius of 4850 km (approximately midway down in the shell) shows the small cross-sectional area of the upwelling flow. The downwelling flow still retains its sheetlike character. At the time of the last snapshot the mean heat flow is 63 mW/m^2 and RMS velocity is 6.0 mm/yr at the outer boundary. The increased thickness of the outer layer of cells appears to have modified the solution only mildly. The mean heat flow is only 4% lower than the previous case.

Power-law relationships for heat flow and surface velocity in terms of the Rayleigh number can be estimated from these results. As

the $R = 100,000$ case is underresolved with an $n = 8$ grid, the $R = 25,000$ and $R = 10^6$ cases are used. For consistency, the first $R = 10^6$ case is selected. Heat flow values of 22.3 and 65.4 mW/m², respectively, for the two cases imply that heat flow is proportional to $R^{0.292}$. RMS surface velocities of 0.601 and 5.82 mm/yr yield an exponent of 0.615 for the velocity power law.

If these power-law relationships are used to extrapolate to a Rayleigh number of 2×10^7 , one obtains a heat flow of 157 mW/m² and a surface velocity of 36.7 mm/yr. Although the surface velocity is similar to what is observed for the earth, the heat flow is roughly twice as high. Correct treatment of the stiff lithosphere in the model would lower the heat flow considerably, however. Furthermore, this scaling is based on cases which had approximately 50% internal heating. One could argue from results of Section 7.4 for partial internal heating that if the internal heating were smaller, the mean velocities would remain essentially unchanged and the heat flow could be smaller by up to a factor of two. Given the simplicity of the model, however, compared with the complexities of compressibility, temperature-dependent rheology, and phase changes associated with the mantle, the agreement is deemed remarkable. These results, particularly the velocity scaling, seem to favor whole-mantle, in contrast to two-layer, convection because of the significantly lower efficiency of two-layer flow.

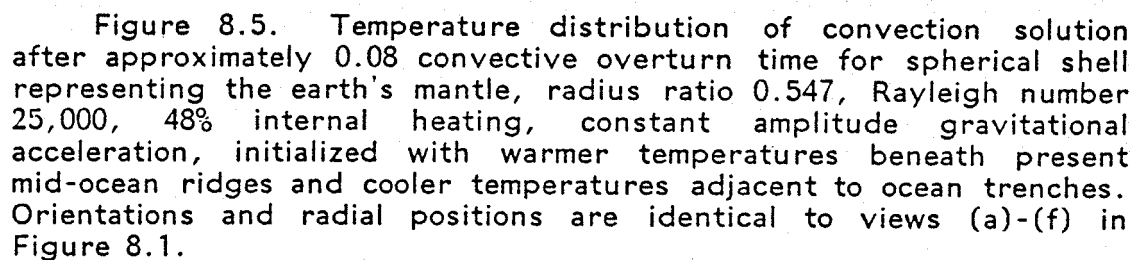


Figure 8.5. Temperature distribution of convection solution after approximately 0.08 convective overturn time for spherical shell representing the earth's mantle, radius ratio 0.547, Rayleigh number 25,000, 48% internal heating, constant amplitude gravitational acceleration, initialized with warmer temperatures beneath present mid-ocean ridges and cooler temperatures adjacent to ocean trenches. Orientations and radial positions are identical to views (a)-(f) in Figure 8.1.

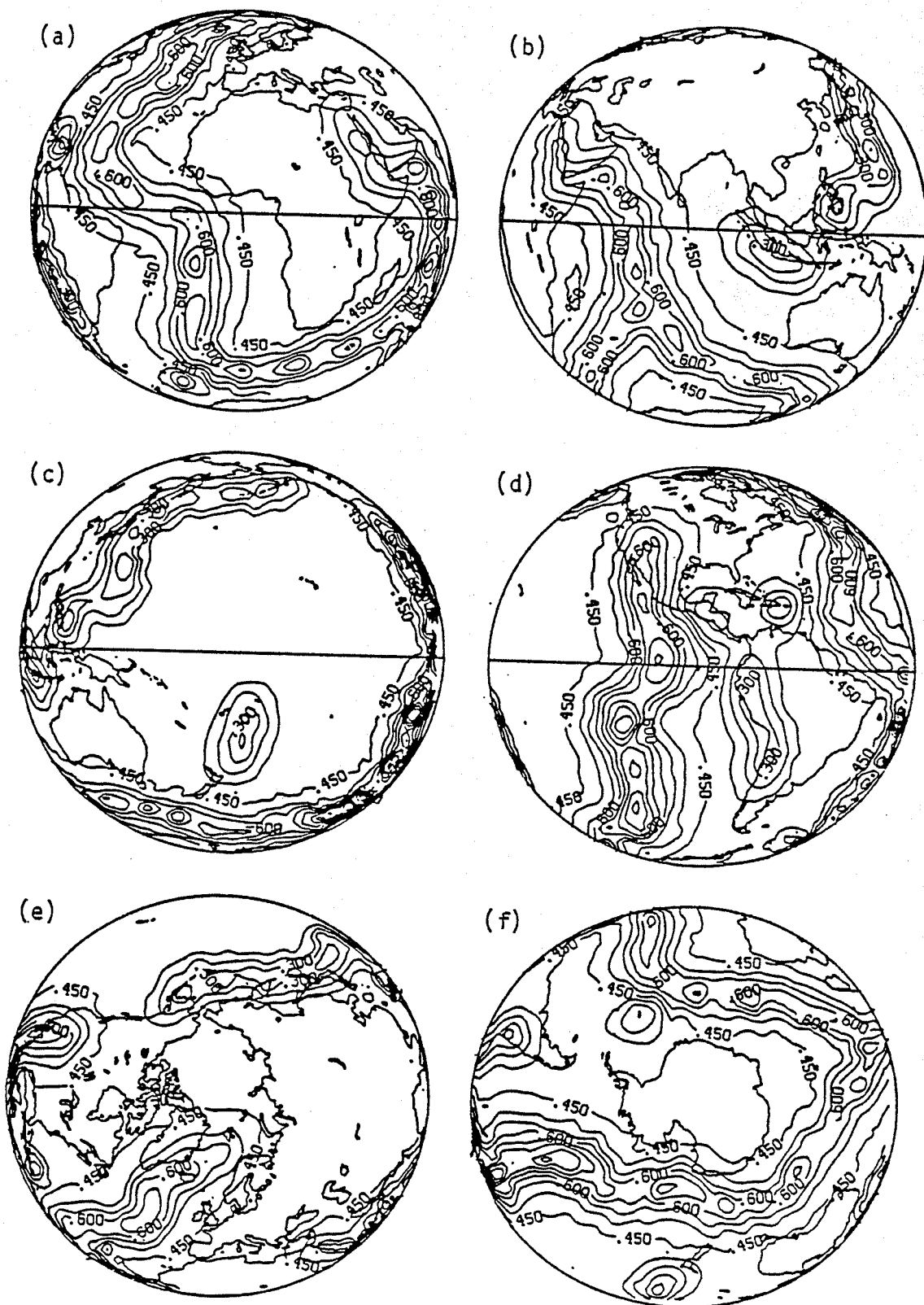


Figure 8.5

Figure 8.6. Convection solution after approximately 0.08 convective overturn time for spherical shell representing the earth's mantle, radius ratio 0.547, Rayleigh number 25,000, 48% internal heating, constant amplitude gravitational acceleration, initialized with warmer temperatures beneath present mid-ocean ridges and cooler temperatures adjacent to ocean trenches. Velocity and temperature fields are shown together in (a)-(l). Orientations and radial positions of views and normalization of temperature contours are identical to views (a)-(l) of Figure 8.1. Maximum velocity for views (a)-(f) is 0.71 mm/yr and for views (g)-(l) is 1.23 mm/yr. Views (m)-(r) have the same orientation as (a)-(f) with radial position of 6368 km and maximum velocity of 0.71 mm/yr.

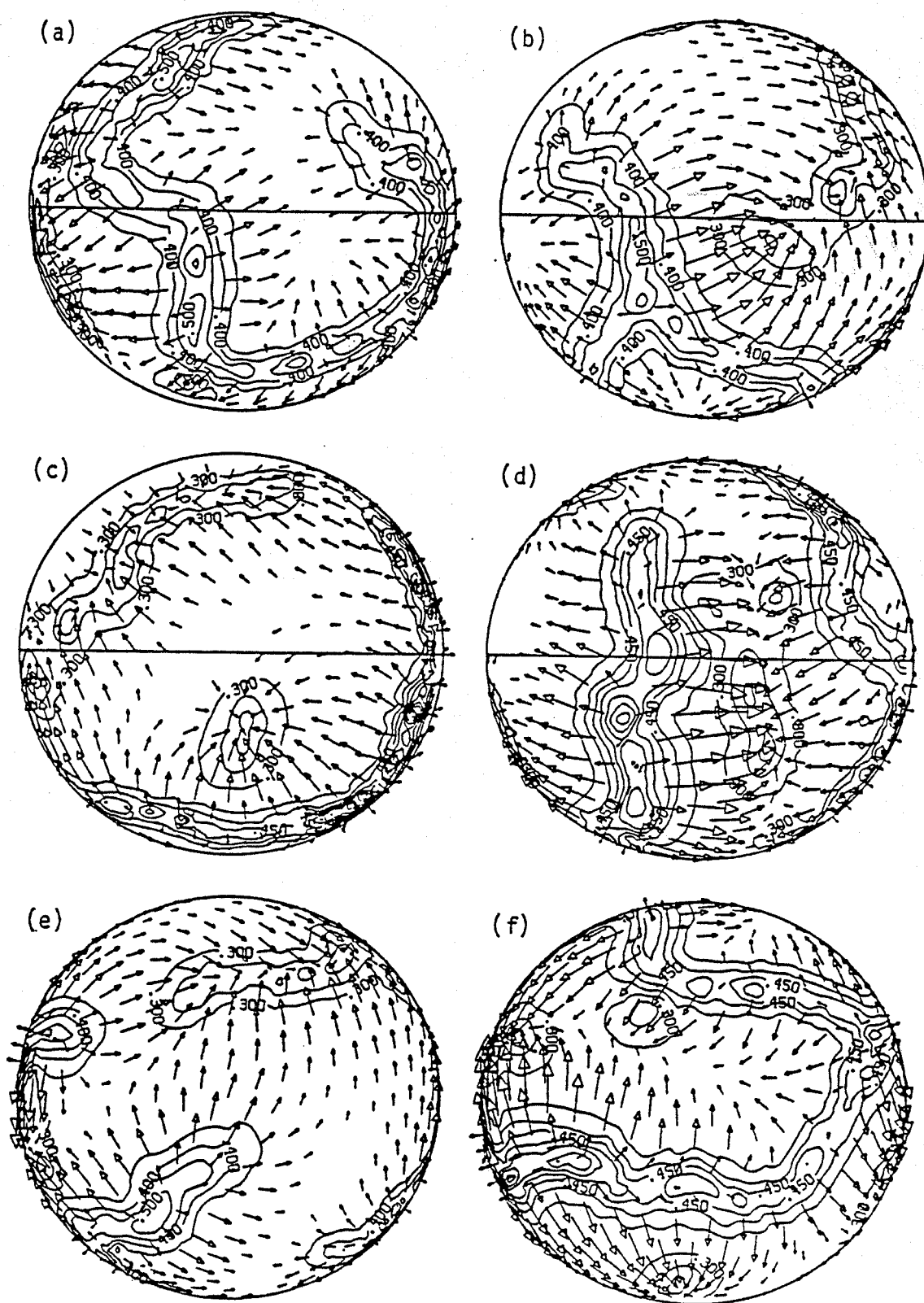


Figure 8.6

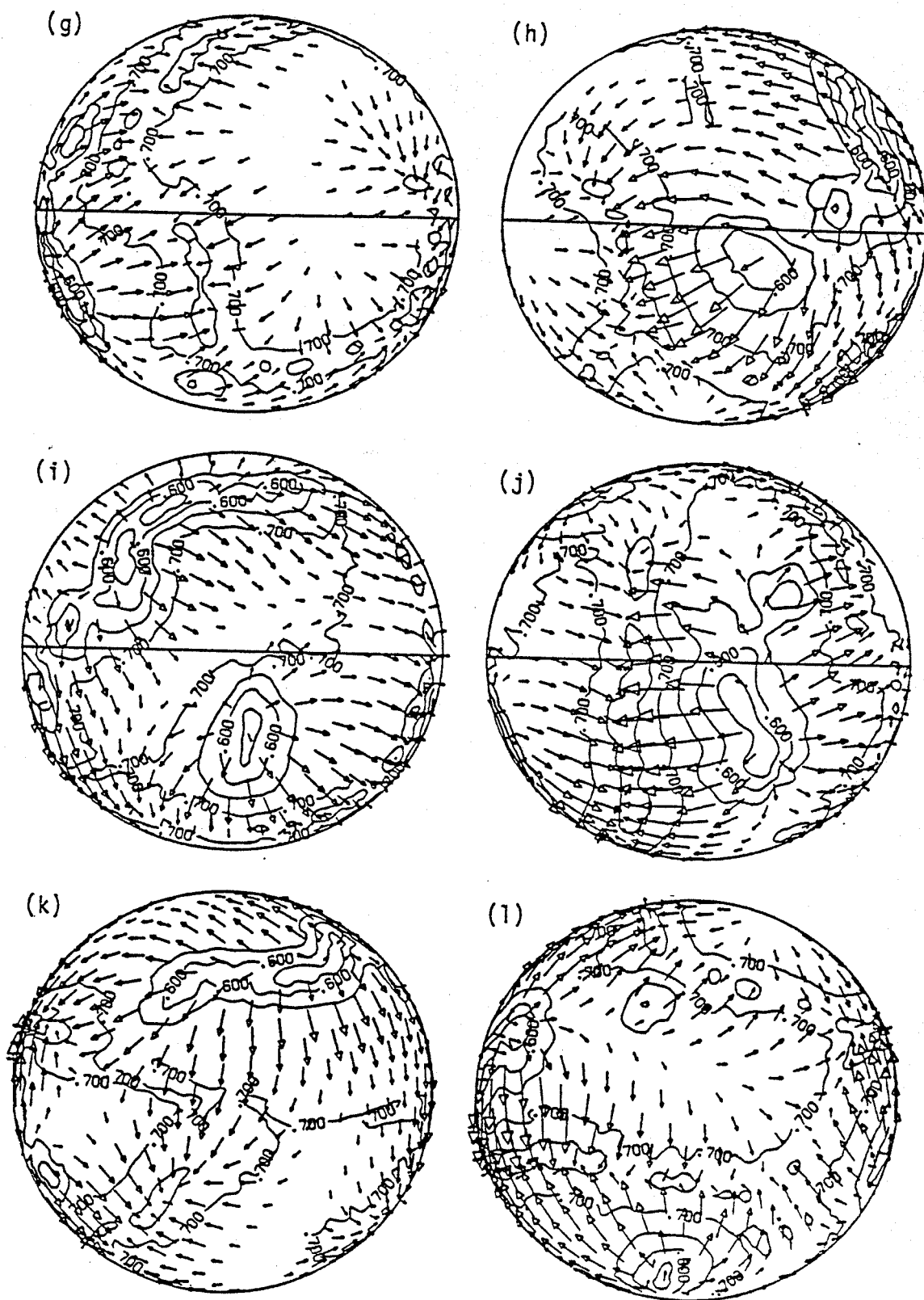


Figure 8.6

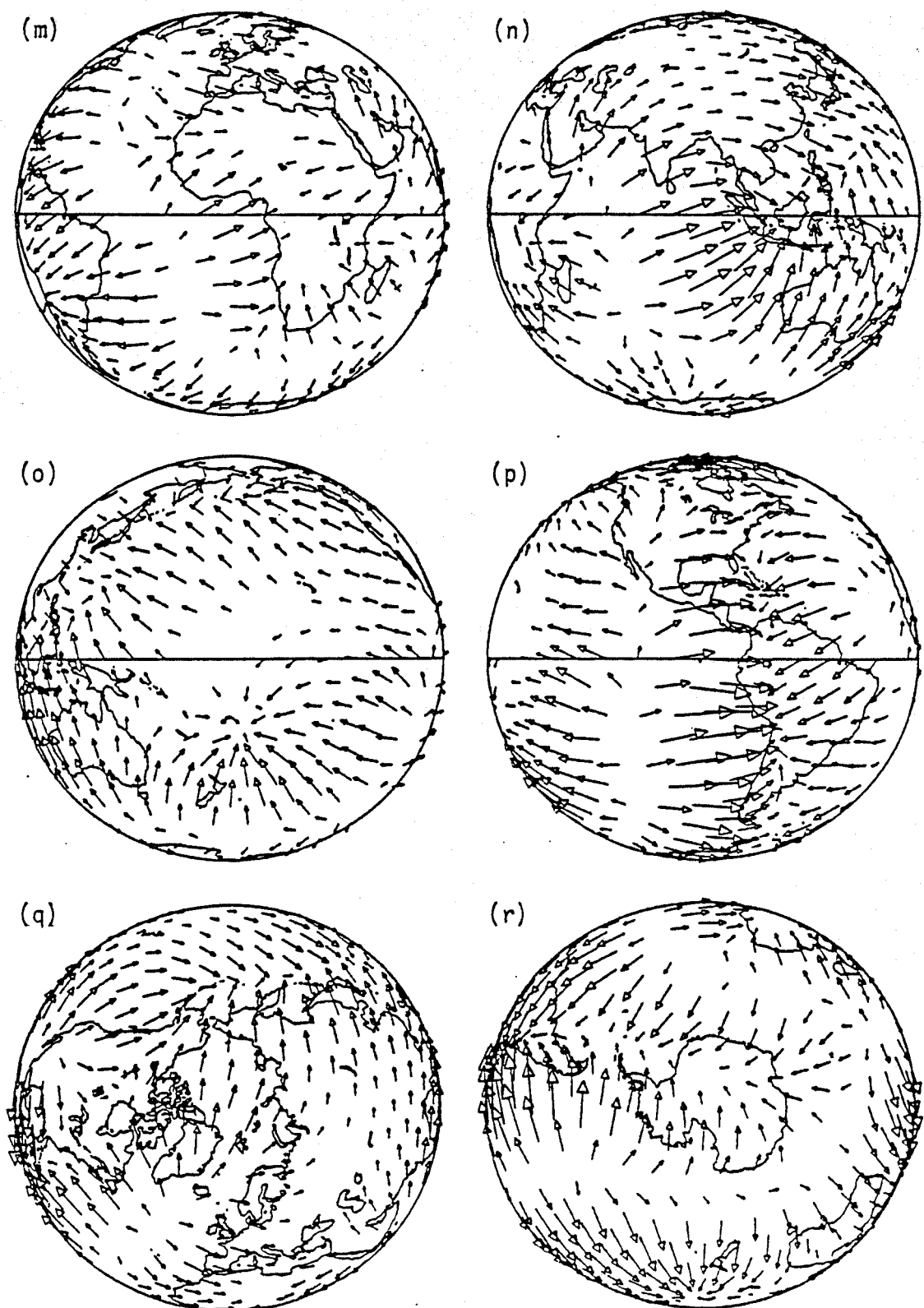


Figure 8.6

Figure 8.7. Same solution as Figure 8.6 except at approximately 0.75 overturn time. Maximum velocity for views (a)-(f) is 1.01 mm/yr and for views (g)-(l) is 1.89 mm/yr.

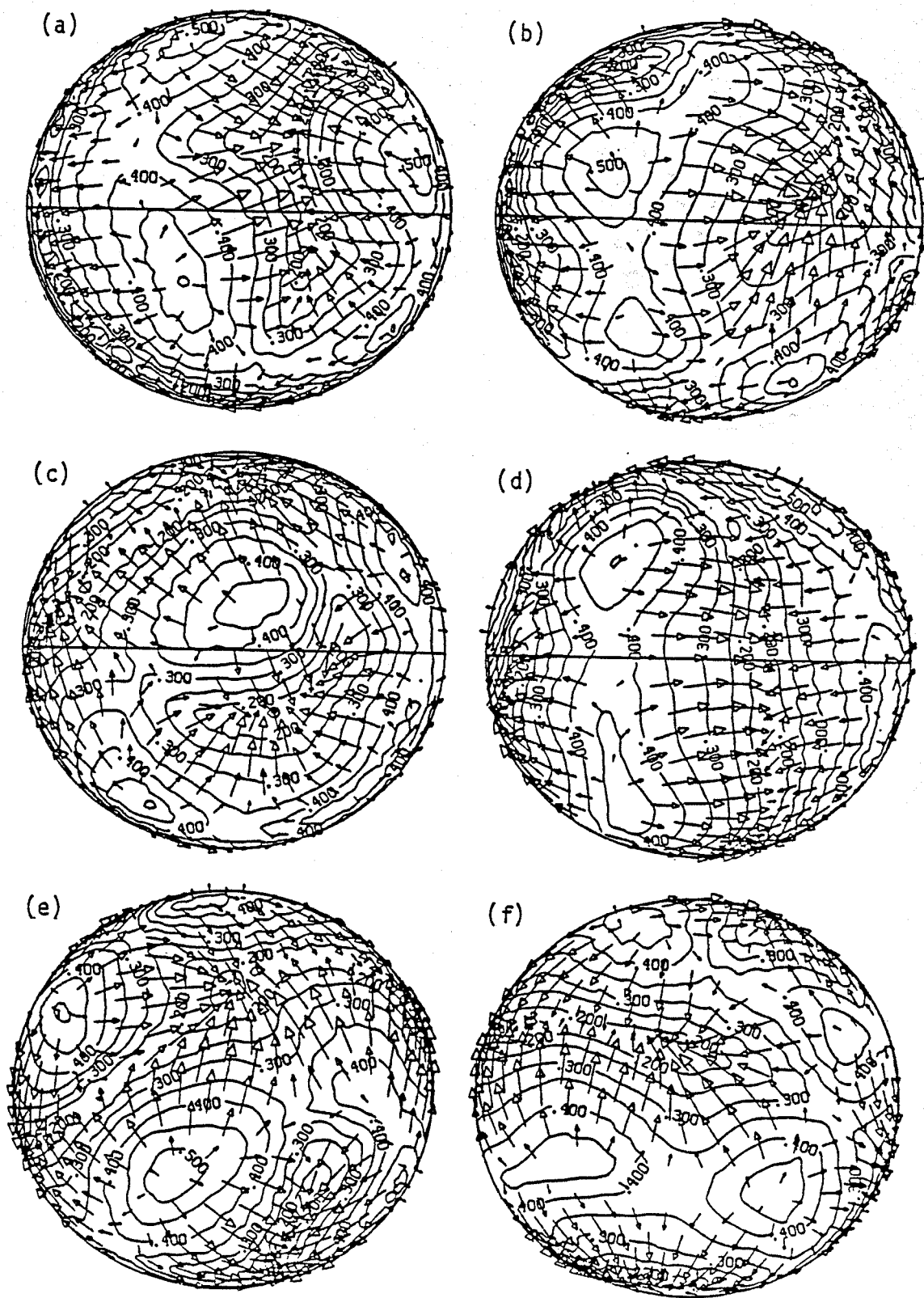


Figure 8.7

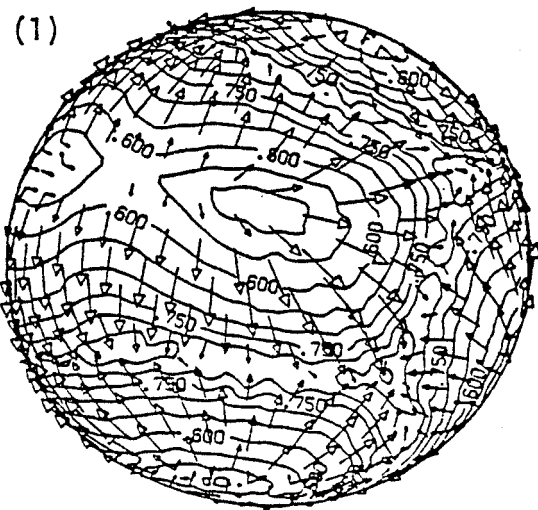
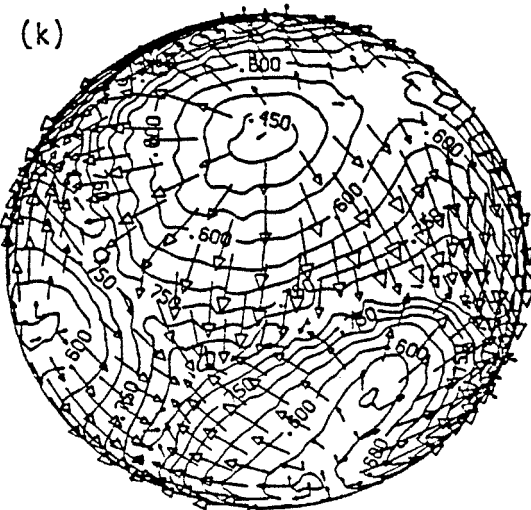
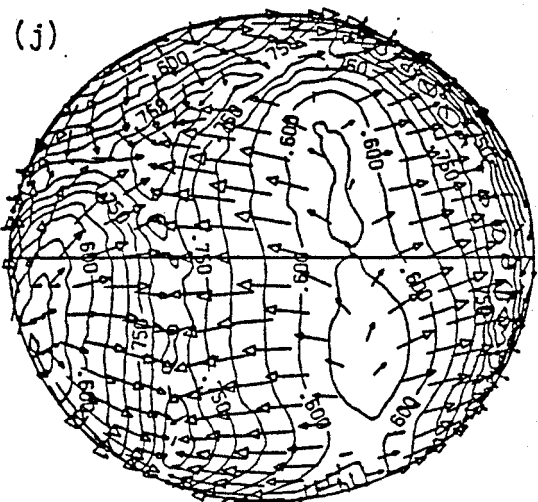
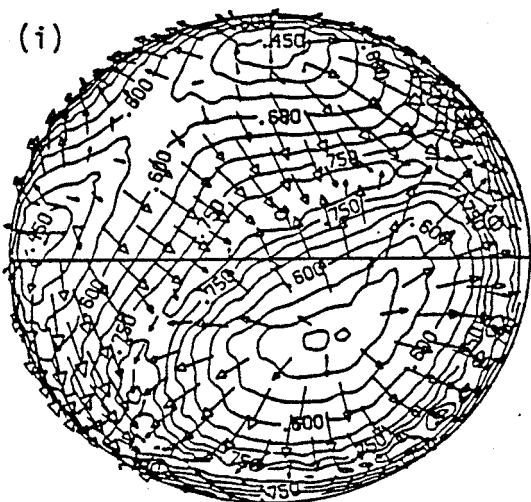
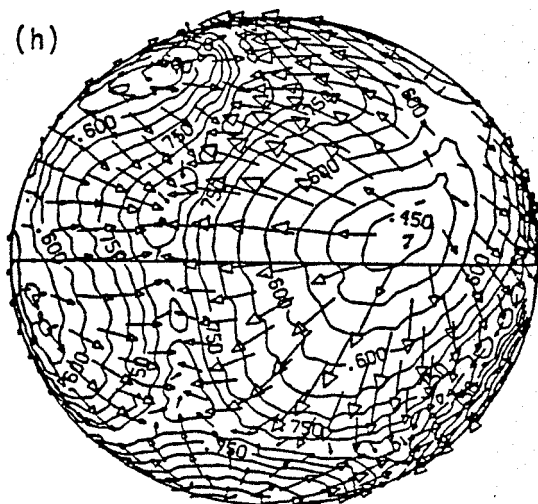
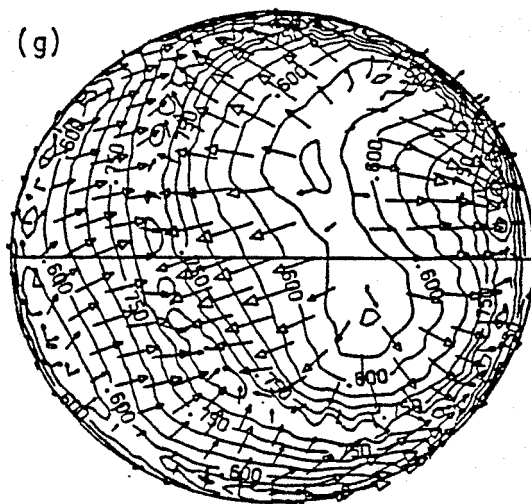


Figure 8.7

Figure 8.8. Same solution as Figure 8.6 except at approximately 2.0 convective overturn times. Maximum velocity for views (a)-(f) is 1.24 mm/yr, for views (g)-(l) is 2.11 mm/yr, and for views (m)-(r) is 1.26 mm/yr.